Nanoscale

Review on the Raman spectroscopy of different types of layered materials

Xin Zhang[*], **Qing-Hai Tan, Jiang-Bin Wu, Wei Shi and Ping-Heng Tan**[*]

Two-dimensional layered materials, such as graphene and transition metal dichalcogenides (TMDs), have been under intensive investigations. The rapid progresses on researches of graphene and TMDs are now stimulating the explorations of different types of layered materials (LMs). Raman spectroscopy has shown its great potentials in characterizations of layer numbers, interlayer coupling and layer-stacking configurations, and will benefit the future explorations of other LMs. Lattice vibrations or Raman spectra of many LMs in bulk have been discussed since 1960s. However, different results were obtained because of differences or limitations in the Raman instruments at early stages. The developments of modern Raman spectroscopy now allow to revisit the Raman spectra of these LMs under the same experimental conditions. Moreover, to our best knowledge, there were limits of detailed review on Raman spectra of these different LMs. Here, we provide a review on Raman spectra of various LMs, including semiconductors, topological insulators, insulators, semi-metal and superconductors. We at first introduce a unified method based on symmetry analysis and polarization measurements to assign the observed Raman modes and characterize the crystal structure of different types of LMs. Then, we revisit and update the positions and assignments of vibration modes by re-measuring the Raman spectra of different types of LMs and by comparing our results to those previous works. We further apply the recent advances on the interlayer vibrations of graphene and TMDs to these various LMs, and obtain shear modulus of many LMs. The observation of the shear modes of LMs in bulk offers an accurate and fast characterization of layer numbers during preparation processes in future by a robust layer-number dependency on the frequencies of the shear modes. We also summaries the recent progresses of the layer-stacking dependence on the intensities of interlayer shear vibrations. Finally, we further review the recent advances on Raman spectroscopy in the characterization of anisotropic LMs, such as black phosphorous and rhenium diselenide. We believe that this review will benefit the future researches on the fundamental physics and potential applications of these various LMs, particularly when they are reduced down to monolayer or multilayers.

1 Introduction

The fast progress of graphene research, fueled by the unique properties of this two-dimensional (2D) material, paved the way to experiments on other layered materials (LMs).[1–3] Transition metal dichalcogenides (TMDs), represented by MX_2 (M = Mo, W; X = S, Se, Te), have received extensive researches on their distinctive electronic and optical properties, and broad applications in devices.[4–9] Bulk MX_2 is an indirect-gap semiconductor, but undergoes the transition to a direct-gap semiconductor in monolayer (1L-) MX_2 because of the absence of interlayer coupling.[4,5] Valley polarization and enhanced excitonic effect have been revealed in 1L-MX_2.[8] MX_2 also shows fine-tuned properties by external perturbations, such as strain, pressure, temperature and electromagnetic field.[10] The advances of TMDs further accelerate the

experiments on different types of LMs. Actually, LMs contain a large family including graphene family, 2D dichalcogenides and 2D oxides, which ranges from insulators (BN, HfS_2 etc.), topological insulators (Bi_2Se_3, Bi_2Te_3 etc.), semiconductors (MX_2, GaSe, GaS, CuS, $SnSe_2$, $PbSnS_2$, GeSe, SnS, $ReSe_2$ etc.), semi-metal (graphene) to superconductors ($NbSe_2$, NbS_2, FeSe, FeTe etc.).[1,10] These LMs differ in atomic composition, crystal structure and electronic structure, which needs an effective way to classify them. One way is based on electronic structure as addressed above. We can also classify these LMs according to symmetry of their crystal structures. For example, graphite, TMDs, GaSe(S), CuS, $SnS(Se)_2$, $TaS(Se)_2$, FeTe(Se), $NbSe_2$ and BN belong to D_{6h}, $SnSe_2$ and $Bi_2Te(Se)_3$ belong to D_{3d}, black phosphorus (BP), GeS(Se) and SnS(Se) belong to D_{2h}, GaTe belongs to C_{2h} and $ReS(Se)_2$ belongs to C_i. Fig. 1 presents five representative LMs from D_{6h}, D_{3d}, D_{2h}, C_{2h} and C_i symmetries. While much advance has been made on LMs who have D_{6h} symmetry, such as graphite and TMDs, those LMs with low symmetry (e.g., D_{3d} and D_{2h}) are just beginning to receive attentions. Re-

State Key Laboratory of Superlattices and Microstructures, Institute of Semiconductors, Chinese Academy of Sciences, Beijing 100083, China. E-mail: zhangxin@semi.ac.cn and phtan@semi.ac.cn.
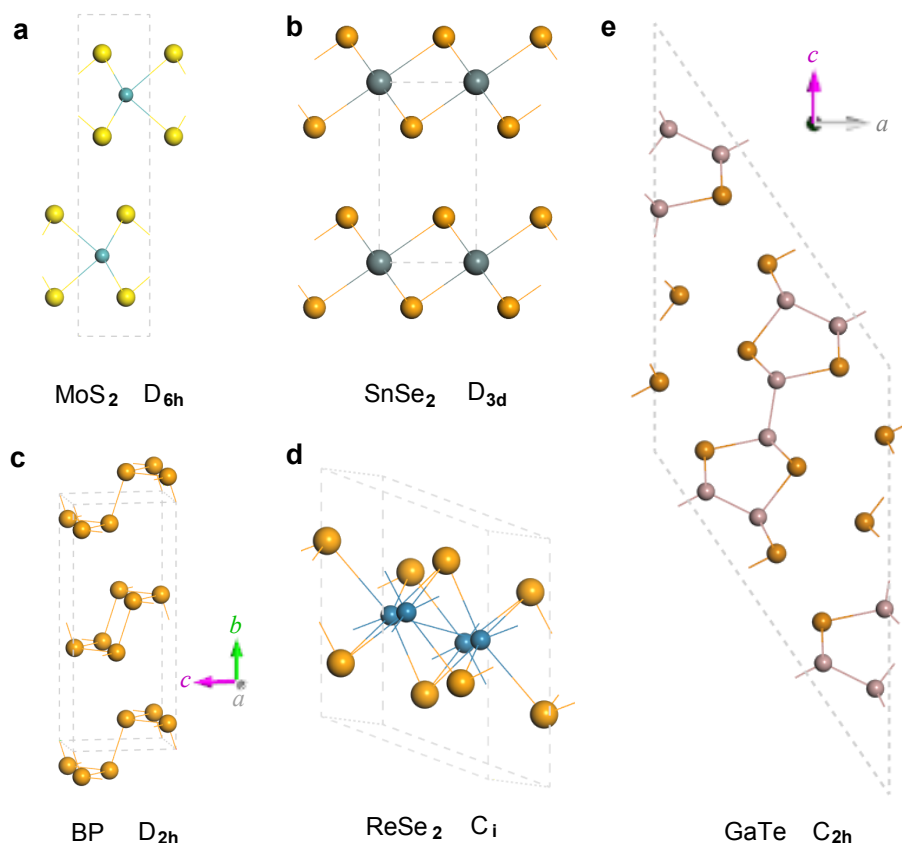
Fig. 1 Atomic structures of five representative LMs (including their symmetries): (a) MoS_2 (D_{6h}), (b) GaSe (D_{3d}), (c) Black phosphorus (BP) (D_{2h}), (d) $ReSe_2$ (C_i) and (e) GaTe (C_{2h}).

cently, BP becomes much popular because it has very high mobility and presents in-plane optical anisotropy. Actually, such in-plane optical anisotropy comes from the symmetry nature of D_{2h} in BP. Thus, similar in-plane optical anisotropy is expected in GeS(Se) and SnS(Se). It should be noticed here that the symmetry is limited within bulk LMs. Because of the absence of out-of-plane transitional symmetry in multilayer structure, those symmetry in bulk LMs will reduce in few layer structures. For example, D_{6h} in bulk TMDs reduces into D_{3h} (odd layer numbers) and D_{3d} (even layer numbers) for few-layer TMDs.[10] The atoms within each layer in LMs are joined together by covalent bonds, while van der Waals interactions keep the layers together, which makes the physical and chemical properties of LMs strongly dependent on their thickness (or layer numbers).[10] The adjacent layers in most LMs are weakly coupled to each other and can be easily exfoliated and isolated down to 1L and few-layers, whose properties are waiting for explorations. In addition, these various LMs could be re-stacked/assembled horizontally or vertically in a chosen sequence to form van der Waals heterostructures (vdWHs), which can offer huge opportunities in designing the

functionalities of such heterostructures.[1,2,11–15] Two or more LMs with similar properties can be alloyed into a new type LMs, namely, 2D alloy, which can offer tunable band gaps for promising applications in nanoelectronics and optoelectronics.[16–19]

Raman spectroscopy now becomes increasingly important in the area of LMs.[10] Raman spectroscopy can reveal the information on crystal structure, electronic structure, lattice vibration and flake thickness of LMs, and be used to probe strain, stability, charger transfer, stoichiometry, stacking orders of LMs.[10] Especially, the unique interlayer vibrations have been widely used to develop a substrate-free layer-number identification of LMs,[19,20] to probe the strength of interlayer coupling in LMs[20,21] and the interface coupling in artificially vdWHs.[13,15] Raman studies of many LMs start from 1960s, but early Raman measurements are mainly limited in bulk LMs.[22–24] Since the successful exfoliations of monolayer graphene in 2004 and monolayer MoS_2 in 2010,[25,26] we should put a fresh look at these bulk LMs. Raman spectra of graphene and TMDs from monolayer, multilayer to bulk are well-known,[10,27] but those of other LMs are still wait-

ing for investigations and revisits. On the other hand, Raman spectra at early stage strongly depend on the using Raman spectroscopy, which usually leads to different peak positions and different profiles with large uncertainty resulting from the sample purity and instrument setup. The much developments of modern Raman spectroscopy now allow us to revisit Raman spectra of these LMs. Moreover, the ultra-low-frequency technique developed by Tan *et al.* in 2012 makes it possible to detect the interlayer vibrations with frequency down to several wavenumbers, which helps us get into the interlayer vibrations of multilayer graphene and TMDs.[13,15,19–21] To meet the growing request of Raman characterization on LMs, we review the Raman spectra of different types of LMs from 1960s. Because of the limitations of early Raman spectroscopy and sample purity, we re-measured the Raman spectra of LMs from several wavenumbers. By comparing our results to those reported in previous papers, we revisit and update the peak positions and corresponding assignments. We at first take three representative LMs who have different symmetries as examples to introduce a unified method to assign the vibration modes by symmetry analysis and polarization measurements. Then we discuss the Raman spectra of different types of LMs by using three subsections: Semiconductors, Topological insulators, and Semi-metal, insulators and superconductors. Furthermore, we apply the recent advances on interlayer vibrations of multilayer graphene and TMDs to many LMs from which we obtain their shear modulus. We also summarize recent advances on the layer-stacking dependence on the intensities of interlayer vibrations. Finally, we review the recent advances on Raman study of in-plane anisotropy in anisotropic LMs, such as black phosphorous and rhenium diselenide. We hope this review will enable a fresh understanding of Raman results in the past fifty years, and be helpful to the studies of these LMs when they are reduced down to monolayer and few layers.

2   Method to assign Raman peaks in LMs

Lattice vibrations are usually denoted by the irreducible representations of the factor group of crystal.[28] From its denotations, we can determine the optical activities of this vibration, i.e., Raman (R) active, Infrared (IR) active or optically silent. The intensity of a Raman-active mode is expressed by the defined Raman tensor (Rt) as:[28] $d\sigma/d\Omega \propto \sum_j |e_s \cdot Rt_j \cdot e_i|^2$, where Rt_j is the jth Raman tensor of the vibration mode. e_i and e_s are the polarization vectors of the incoming and scattered photons, respectively. e_i (e_s) along x,y,z is $(1,0,0),(0,1,0),(0,0,1)$, respectively. One can use four letters, A(BC)D, to represent the different scattering configurations in Raman measurements. "A" and "D" are the propagation directions of incoming and scattered photons, while "B" and "C" are the polarized directions of incoming (e_i) and scattered (e_s) photons.

Under the back scattering condition, "A" and "D" are fixed along Z and $\overline{Z}$ (the opposite direction of Z), respectively. Thus, $Z(BC)\overline{Z}$ can simply be denoted by BC. There are four scattering configurations under back scattering condition, XX, XY, YX and YY. XX and YY are called unpolarized configurations, while XY and YX are polarized configurations. Raman tensors can be obtained in the standard textbooks and review articles.[28,29] Next, we will take MoS$_2$ (D$_{6h}$),[20,30] Bi$_2$Se$_3$ (D$_{3d}$)[31–33] and GeSe (D$_{2h}$)[34,35] as examples to introduce the method to assign Raman peaks in the Raman spectra.

The factor group at Γ point is the point group which the crystal belongs to,[28] thus, it is D_{6h} for bulk MoS$_2$, D_{3d} for bulk Bi$_2$Se$_3$ and D_{2h} for bulk GeSe. Because there are two Mo atoms and four S atoms in the unit cell of bulk MoS$_2$, 18 normal vibration modes at Γ point are expected and denoted by:[36,37] $\Gamma = A_{1g} + 2A_{2u} + 2B_{2g} + B_{1u} + E_{1g} + 2E_{1u} + 2E_{2g} + E_{2u}$, where 3 acoustic modes are $A_{2u} + E_{1u}$, 15 optical modes are $A_{1g} + A_{2u} + 2B_{2g} + B_{1u} + E_{1g} + E_{1u} + 2E_{2g} + E_{2u}$. Raman and infrared active modes can be determined from the character table for D_{6h} (Please see Table S1 in ESI†). Those irreducible representations (marked in red in Table S1 in ESI†) transform as a quadratic term of x,y,z (e.g., $x^2 \pm y^2$, z^2, xz, yz and xy) are Raman active, while those (marked in blue in Table S1 in ESI†) as a linear term (i.e., x, y, z) are infrared active. The remaining irreducible representations are optically silent which principally cannot be detected by Raman or infrared spectroscopy.[28,37] Thus, for bulk MoS$_2$, A_{2u} and E_{1u} among 15 optical modes are infrared active, while A_{1g}, E_{1g} and $2E_{2g}$ are Raman active, and $2B_{2g}$, B_{1u} and E_{2u} are optically silent. We observed three modes, $\sim$32.5 cm^{-1}, $\sim$383.3 cm^{-1} and $\sim$408.6 cm^{-1} under XX configuration, as shown in Fig. 1. However, the mode $\sim$408.6 cm^{-1} almost disappears under YX configuration, while the other two modes keep their intensity almost unchanged. The polarization-dependent intensity of a Raman mode is determined by its Raman tensor (Rt). The Raman tensors (Rt) of A_{1g}, E_{1g} and E_{2g} are presented, respectively, as follows:[29]

$$A_{1g}(D_{6h}): \begin{pmatrix} a & 0 & 0 \\ 0 & a & 0 \\ 0 & 0 & b \end{pmatrix}$$

$$E_{1g}(D_{6h}): \begin{pmatrix} 0 & 0 & 0 \\ 0 & 0 & c \\ 0 & c & 0 \end{pmatrix}, \begin{pmatrix} 0 & 0 & -c \\ 0 & 0 & 0 \\ -c & 0 & 0 \end{pmatrix}$$

$$E_{2g}(D_{6h}): \begin{pmatrix} 0 & d & 0 \\ d & 0 & 0 \\ 0 & 0 & 0 \end{pmatrix}, \begin{pmatrix} d & 0 & 0 \\ 0 & -d & 0 \\ 0 & 0 & 0 \end{pmatrix}$$

Both E_{1g} and E_{2g} have two Raman tensors (Rt_1 and Rt_2) because they are doubly degenerate within xy plane. The intensity of A_{1g} mode, I(A_{1g}), under XX (e_s=(1,0,0), e_i=(1,0,0)) configuration is I(A_{1g})$\propto|e_s \cdot Rt \cdot e_i|^2$=$a^2$, while under YX
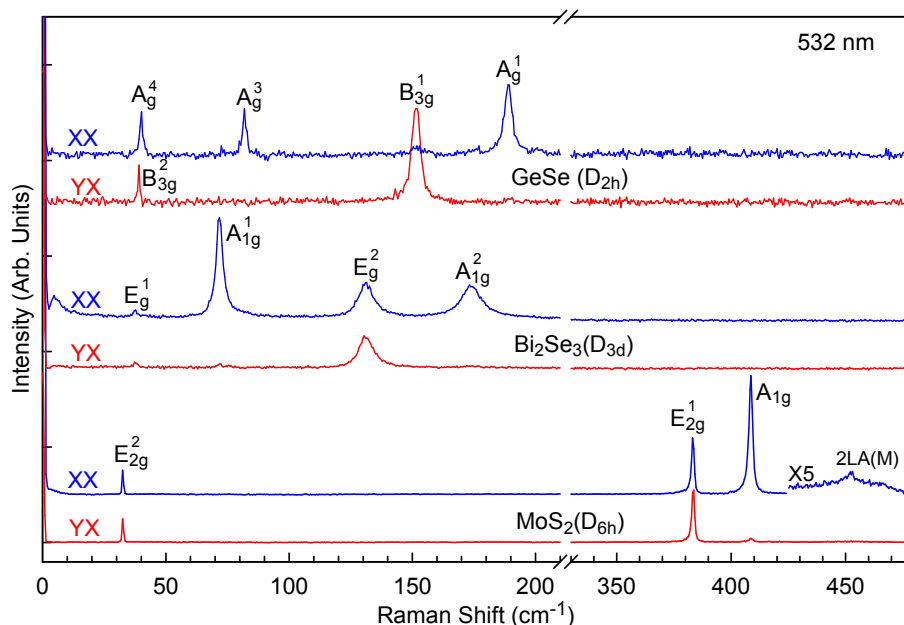
Fig. 2 Raman spectra of three representative bulk materials, GeSe (D_{2h}), Bi$_2$Se$_3$ (D_{3d}) and MoS$_2$ (D_{6h}), under XX and YX polarization configurations.

(e_s=(0,1,0), e_i=(1,0,0)) configuration I(A_{1g}) = 0. It suggests that the A_{1g} mode will disappear when the polarization configuration is changed from XX to YX. Thus, the mode ∼408.6 cm^{-1} is assigned as A_{1g}. In a similar way, we have the expression of I(E_{2g})∝$|e_s \cdot Rt_1 \cdot e_i|^2 + |e_s \cdot Rt_2 \cdot e_i|^2 = d^2$ for both XX and YX configuration, which suggests that the E_{2g} mode will keep their intensity unchanged. Here Rt_1 and Rt_2 are two Raman tensors of the E_{2g} mode. Thus, we assign the two modes at ∼32.5 cm^{-1} and ∼383.3 cm^{-1} as E_{2g}. We further use number superscripts of "1" and "2" for E_{2g} to distinguish the modes with same symmetry, i.e., E_{2g}^1 (∼383.3 cm^{-1}) and E_{2g}^2 (∼32.5 cm^{-1}). This can be generally applicable to the other modes. It should be noted that the E_{1g} mode can not be observed for both XX and YX configuration because I(E_{1g}) = 0. The broad peak at ∼452.0 cm^{-1} comes from 2LA(M).[38]

For bulk Bi$_2$Se$_3$, there are 15 normal vibration modes, which are expressed as follows: $\Gamma = 2A_{1g} + 3A_{2u} + 2E_g + 3E_u$, where $2A_{1g}$ and $2E_g$ are Raman active, $3A_{2u}$ and $3E_u$ are infrared active. The Raman tensors (Rt) of the A_{1g} and E_g modes are presented as follows:[29]

$$A_{1g}(D_{3d}) : \begin{pmatrix} a & 0 & 0 \\ 0 & a & 0 \\ 0 & 0 & b \end{pmatrix}$$

$$E_g(D_{3d}) : \begin{pmatrix} c & 0 & 0 \\ 0 & -c & d \\ 0 & d & 0 \end{pmatrix}, \begin{pmatrix} 0 & -c & -d \\ -c & 0 & 0 \\ -d & 0 & 0 \end{pmatrix}$$

Based on the above Raman tensors, the E_g mode can be observed under both XX and YX configuration, while the A_{1g} mode is observable only under XX configuration. Thus, we assign the observed four modes in Fig. 1 as E_g^1 (∼37.1 cm^{-1}), A_{1g}^1 (∼71.6 cm^{-1}), E_g^2(∼130.8 cm^{-1}) and A_{1g}^2 (∼173.6 cm^{-1}).[33]

For bulk GeSe, there are two layers in its unit cell, each of them contains four atoms.[39,40] Thus, 24 normal vibration modes are expected and denoted as follows: $\Gamma = 4A_g + 4B_{1u} + 2B_{1g} + 2A_u + 4B_{2g} + 4B_{3u} + 2B_{3g} + 2B_{2u}$, where $4A_g$, $2B_{1g}$, $4B_{2g}$ and $2B_{3g}$ are Raman active.[34] Their Raman tensors (Rt) are as follows:[29]

$$A_g(D_{2h}) : \begin{pmatrix} a & 0 & 0 \\ 0 & b & 0 \\ 0 & 0 & c \end{pmatrix}$$

$$B_{1g}(D_{2h}) : \begin{pmatrix} 0 & d & 0 \\ d & 0 & 0 \\ 0 & 0 & 0 \end{pmatrix}$$

$$B_{2g}(D_{2h}) : \begin{pmatrix} 0 & 0 & e \\ 0 & 0 & 0 \\ e & 0 & 0 \end{pmatrix}$$

$$B_{3g}(D_{2h}) : \begin{pmatrix} 0 & 0 & 0 \\ 0 & 0 & f \\ 0 & f & 0 \end{pmatrix}$$

We should note here that the scattering configuration, A(BC)D, is defined in the experimental coordinates (x, y, z), but the above Raman tensors (Rt) are actually defined in the crystal coordinates (a, b, c). For MoS_2 and Bi_2Se_3, the direction of the layer stacking is along c, which is set along z axis. Thus, the crystal and experimental coordinates are same. However, the direction of the layer stacking in GeSe ($a = 10.825$ Å, $b = 3.833$ Å, $c = 4.388$ Å) is along a which is taken along z axis.[41] Thus, the Raman tensor (Rt) needs to be converted from the crystal coordinates to the experimental coordinates, and the new Raman tensor (Rt') in the experimental coordinates can be obtained by:

$$Rt' = TRtT^{-1}, \qquad (1)$$

where T is the transform matrix from the crystal coordinates (a, b, c) to the experimental coordinates (x, y, z). T^{-1} is the inverse matrix of T. Here, we need to clockwise rotate $\pi/2$ about b axis. Thus, T is

$$T : \begin{pmatrix} 0 & 0 & -1 \\ 0 & 1 & 0 \\ 1 & 0 & 0 \end{pmatrix}$$

and thus we obtain Rt' by equation (1) as follows:

$$A_g(D_{2h}) : \begin{pmatrix} c & 0 & 0 \\ 0 & b & 0 \\ 0 & 0 & a \end{pmatrix}$$

$$B_{1g}(D_{2h}) : \begin{pmatrix} 0 & 0 & 0 \\ 0 & 0 & d \\ 0 & d & 0 \end{pmatrix}$$

$$B_{2g}(D_{2h}) : \begin{pmatrix} 0 & 0 & -e \\ 0 & 0 & 0 \\ -e & 0 & 0 \end{pmatrix}$$

$$B_{3g}(D_{2h}) : \begin{pmatrix} 0 & -f & 0 \\ -f & 0 & 0 \\ 0 & 0 & 0 \end{pmatrix}$$

We observed three modes under XX configuration, ~ 40 cm^{-1}, ~ 82 cm^{-1} and ~ 188 cm^{-1}, while another two modes under YX configuration, ~ 39 cm^{-1} and ~ 151 cm^{-1}, as shown in Fig. 1. Based on their Raman tensors (Rt'), we have I$(A_g) = c^2$, I$(B_{1g}) = 0$, I$(B_{2g}) = 0$ and I$(B_{3g}) = 0$ under XX configuration, and I$(A_g) = 0$, I$(B_{1g}) = 0$, I$(B_{2g}) = 0$ and I$(B_{3g}) = f^2$ under YX configuration. Thus, we assign the five modes as A_g^4 (~ 40 cm^{-1}), A_g^3 (~ 82 cm^{-1}) and A_g^1 (~ 188 cm^{-1}), B_{3g}^2 (~ 39 cm^{-1}) and B_{3g}^1 (~ 151 cm^{-1}).[34] the four A_g modes can be observed under XX configuration from the symmetry classification. However, we just observed three of them by the 532-nm excitation. Actually, another mode ~ 175 cm^{-1} is detected by

the 633-nm excitation and assigned as A_g^2, as shown in Fig. S1 in ESI†. We can also convert the experimental coordinates (x, y, z) to the crystal coordinates (a, b, c). Under the clockwise rotation of $\pi/2$ about b axis, we have $a = z, b = y, c = -x$. Thus, the scattering configurations, $Z(XX)\overline{Z}$ and $Z(YX)\overline{Z}$ are changing into $a(cc)\overline{a}$ and $a(bc)\overline{a}$, respectively. Thus, based on the Raman tensors (Rt), the A_g mode appears under $a(cc)\overline{a}$ ($Z(XX)\overline{Z}$) while the B_{3g} mode under $a(bc)\overline{a}$ ($Z(YX)\overline{Z}$). The above two methods are equivalent. It should be noted here that BP ($a = 3.314$ Å, $b = 10.478$ Å, $c = 4.376$ Å) also belongs to D_{2h}.[42] However, the direction of layer stacking is along b axis. Under the counterclockwise rotation of $\pi/2$ about a axis, we have $a = x, b = z, c = -y$. Thus, the scattering configurations, $Z(XX)\overline{Z}$ and $Z(YX)\overline{Z}$ are changed into $b(aa)\overline{b}$ and $b(ca)\overline{b}$, respectively. Based on the Raman tensors (Rt), the A_g mode appears under $b(aa)\overline{b}$ ($Z(XX)\overline{Z}$) while the B_{2g} mode under $b(ca)\overline{b}$ ($Z(YX)\overline{Z}$). Review on the Raman spectrum of black phosphorous will be presented in the 5th section.

Based on symmetry analysis and polarization Raman measurements, we can effectively assign the peaks observed in Raman spectra. In many cases, the number of peaks in a Raman spectrum is far smaller than the number of Raman active modes. The appearance of a Raman active mode is still affected by several factors: (1) Scattering configuration. Besides the Raman activity of a Raman mode, proper scattering configuration is necessary for its appearance in the Raman spectrum, as addressed above. For example, the E_{1g} mode of bulk MoS_2 cannot be detected under the back-scattering configuration. (2) Electron-phonon coupling. The intensity of a Raman active mode is proportional to the strength square of electron-phonon coupling in its Raman processes. (3) Excitation energy. One can tune the laser excitation energy to match the electron transition energy of the sample to enhance the Raman intensity of some Raman modes. (4) Instrument throughput. Many components in a Raman system exhibit wavelength-dependent efficiency for the laser excitation and Raman signal, and finally affect its signal throughput. For example, the Raman filter can determine the limitations in probing the ultralow-frequency modes.

3 Raman spectra of different types of bulk LMs

3.1 Semiconductors

Bulk TMDs, such as MoS_2, WS_2, WSe_2 and $MoSe_2$, have attracted much attentions in electronic and optical properties.[8] Recent advances on TMDs are collected in themed issue of 2D transition metal dichalcogenide nanosheets in Chemical Society Reviews.[10,43–56] Especially, ref. 10 reviewed the Raman scattering of TMDs from monolayer, multilayer to bulk materials. MoS_2, WS_2, WSe_2 and $MoSe_2$ have D_{6h} symmetry. Based on the symmetry analysis (Section 2), A_{1g}, E_{1g}
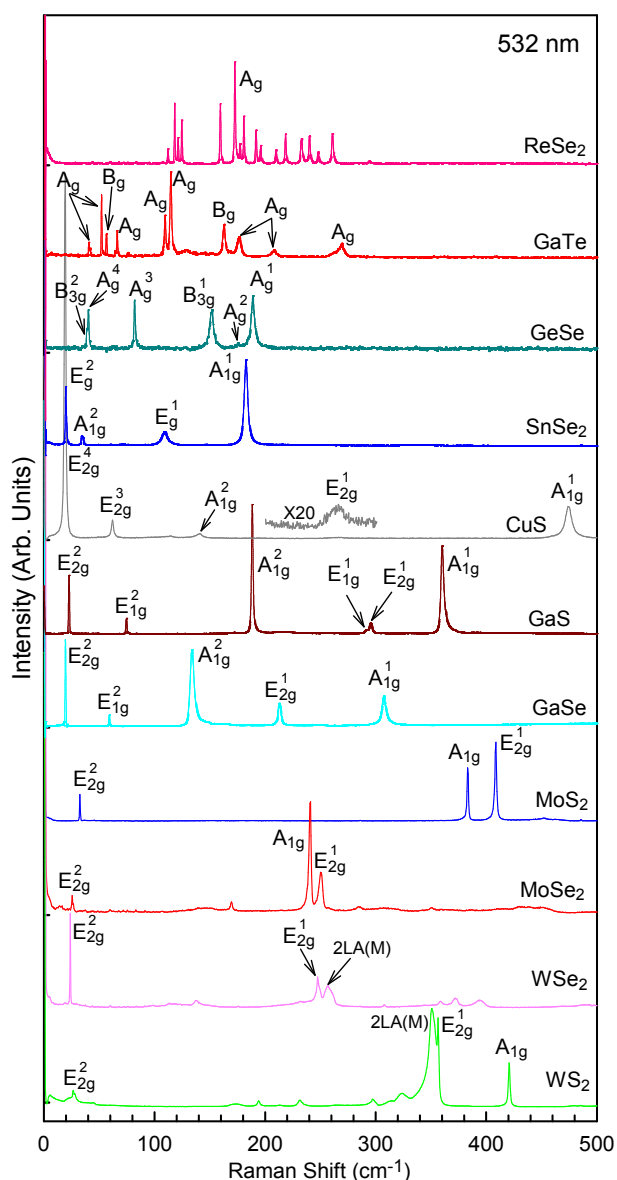
Fig. 3 Raman spectra of bulk WS_2, WSe_2, $MoSe_2$, MoS_2, GaSe, GaS, CuS, $SnSe_2$, GeSe, GaTe and $ReSe_2$.

and $2E_{2g}$ are expected in the Raman spectra of these TMDs. However, only A_{1g} and $2E_{2g}$ will come up under the backscattering configuration. The Raman spectra of MoS_2, WS_2, WSe_2 and $MoSe_2$ are presented in Fig. 3. Although they share similar crystal structure, each of them shows distinctive Raman spectrum (Fig. 3). A_{1g} and $2E_{2g}$ has been detected and assigned as follows,[10] MoS_2: E_{2g}^2 ($\sim$32.5 cm^{-1}), E_{2g}^1 ($\sim$383.3 cm^{-1}), A_{1g} ($\sim$408.6 cm^{-1}); WS_2: E_{2g}^2 ($\sim$27.5 cm^{-1}), E_{2g}^1 ($\sim$356.5 cm^{-1}), A_{1g} ($\sim$420.0 cm^{-1}); WSe_2: E_{2g}^2 ($\sim$23.8 cm^{-1}), E_{2g}^1 ($\sim$248.0 cm^{-1}), A_{1g} ($\sim$251.0 cm^{-1}) (detected by

632-nm excitation. See Fig. S1 in ESI†); $MoSe_2$:[57,58] E_{2g}^2 ($\sim$25.5 cm^{-1}), E_{2g}^1 ($\sim$285.0 cm^{-1}), A_{1g} ($\sim$240.6 cm^{-1}). Besides the phonons at Γ point in the Brillouin zone (BZ), those from the M point also contribute to the observed Raman peaks in these TMDs. The mode $\sim$452.0 cm^{-1} in MoS_2, $\sim$351.4 cm^{-1} in WS_2 and $\sim$351.4 cm^{-1} in WSe_2 are assigned to the overtone of LA phonons at the M point (2LA(M)) under the resonant excitation condition.[10,38,59,60] Actually, more combination modes from phonons at M point are revealed, for example, $\sim$174 cm^{-1}, $\sim$231 cm^{-1} and $\sim$297 cm^{-1} in WS_2 are assigned to LA(M), A_{1g}(M) and 2LA(M)-E_{2g}^2(M), respectively.[60] However, many peaks can not be assigned, for example, $\sim$193 cm^{-1}, $\sim$313 cm^{-1} and $\sim$324 cm^{-1} in WS_2; $\sim$138 cm^{-1}, $\sim$307 cm^{-1}, $\sim$359 cm^{-1}, $\sim$372 cm^{-1} and $\sim$394 cm^{-1} in WSe_2; $\sim$250.5 cm^{-1} in $MoSe_2$. These peaks need further clarifications. Those modes with frequencies close to the above un-assigned modes in 1L-TMDs were assigned by Zhang *et al.* based on their phonon dispersions as follows: $\sim$193 cm^{-1} ($E'(M)^{LO_2}$-LA(M)) and $\sim$325 cm^{-1} ($E''(M)$) in WS_2; $\sim$136 cm^{-1} ($A_1'(M)$-LA(M)), $\sim$374 cm^{-1} ($E'(M)^{LO_2}$+LA(M)) and $\sim$394 cm^{-1} (3LA(M)) in WSe_2.[10]

Bulk GaSe is well known as a second-order nonlinear-optical materials.[61] The thin film of GaSe has been used for the fabrication of photo-detectors.[62] Both GaSe (β-GaSe) and GaS (β-GaS) belong to D_{6h}. Single tetralayer is composed of four atomic sheets arranged along c axis in the sequence of Se(S)-Ga-Ga-Se(S), and there are two tetralayers in their unit cell of bulk materials. 24 normal vibration modes at Γ are expected and expressed as:[23,63] $\Gamma= 2A_{1g} + 2A_{2u} + 2B_{2g} + 2B_{1u} + 2E_{1g} + 2E_{1u} + 2E_{2g} + 2E_{2u}$. There are six non-degenerate Raman-active modes ($2A_{1g}$, $2E_{2g}$, $2E_{1g}$) and two infrared-active modes(E_{1u}, A_{2u}).[22] $2A_{1g}$, $2E_{2g}$, $2E_{1g}$ in GaSe (measured at 77 K) and GaS (measured at room temperature) has been assigned by Irwin *et al.*.[22] Based on our polarization measurements, vibration modes in Fig. 3 for GaSe and GaS are assigned as follows, GaSe: E_{2g}^2 ($\sim$19.3 cm^{-1}), E_{1g}^2 ($\sim$59.2 cm^{-1}), A_{1g}^2 ($\sim$134.0 cm^{-1}), E_{1g}^1 ($\sim$209.3 cm^{-1}) (detected by 633-nm excitation. See Fig. S1 in ESI†), E_{2g}^1 ($\sim$212.6 cm^{-1}), A_{1g}^1 ($\sim$307.5 cm^{-1}); GaS: E_{2g}^2 ($\sim$22.4 cm^{-1}), E_{1g}^2 ($\sim$74.8 cm^{-1}), A_{1g}^2 ($\sim$188.5 cm^{-1}), E_{1g}^1 ($\sim$291.2 cm^{-1}), E_{2g}^2 ($\sim$295.3 cm^{-1}), A_{1g}^1 ($\sim$361.1 cm^{-1}). All the modes in GaSe blueshift relative to the corresponding modes in GaS, which can be attributed to much large mass of selenium than sulphur atoms.[22] It should be noted that $\sim$209.3 cm^{-1} (E_{1g}^1) mode did not appear by the 532-nm excitation, but can be clearly observed by 632-nm excitation (See Fig. S1 in ESI†). Different from Irwin *et al.*'s Raman result, we found that the A_{1g}^2 ($\sim$134.0 cm^{-1}) mode (Fig. 3) is with an asymmetric profile. Particularly, we found two peaks close to A_{1g}^2 ($\sim$188.5 cm^{-1}) in GaS (Fig. 3), lying at $\sim$ 171.9 cm^{-1} and $\sim$ 216.1 cm^{-1}, respec-

tively. The origins of the asymmetric A_{1g}^2 mode in GaSe and two modes close to A_{1g}^2 in GaS need further research. Another polytype GaSe, denoted by ε-GaSe, has different stacking tetralayer from β-GaSe.[22] ε-GaSe has D_{3h} symmetry with two tetralayers in the unit cell. Compared with β-GaSe, the Raman spectrum of ε-GaSe shows a new mode $\sim$252.1 cm^{-1}, which comes from the LO-TO splitting of the $E^{'}$ mode.[22] The absence of this mode suggests that our sample is β-GaSe.

CuS belongs to D_{6h} above 55 K, but decreases to D_{2h} below 55 K.[64] Its unit cell contains 12 atoms, thus 36 normal vibration modes at Γ are expected. Above 55 K, 36 normal vibration modes are expressed as:[64] $\Gamma= 2A_{1g} + 4A_{2u} + 4B_{2g} + 2B_{1u} + 2E_{1g} + 4E_{1u} + 4E_{2g} + 2E_{2u}$, where $2A_{1g}$, $2E_{1g}$ and $4E_{2g}$ are Raman active. Seven Raman peaks has been observed by Ishii $et~al.$, 19 cm^{-1}, 62 cm^{-1}, 65 cm^{-1}, 112 cm^{-1}, 142 cm^{-1}, 267 cm^{-1}, 457 cm^{-1}.[64] They only assigned two modes, 19 cm^{-1} and 457 cm^{-1}, as E_{2g} and A_{1g}, respectively. We observed three modes ($\sim$19.3 cm^{-1}, $\sim$61.8 cm^{-1} and $\sim$266.3 cm^{-1}) under 532-nm excitation and one mode ($\sim$65.0 cm^{-1}) under 633-nm excitation (See Fig. S1 in ESI†) under both XX and YX configurations. These four modes correspond to $4E_{2g}$, which are denoted as E_{2g}^4($\sim$19.3 cm^{-1}), E_{2g}^3($\sim$61.8 cm^{-1}), E_{2g}^2($\sim$65.0 cm^{-1}) and E_{2g}^1 ($\sim$266.3 cm^{-1}). Three modes, $\sim$113.0 cm^{-1}, $\sim$140.0 cm^{-1} and $\sim$474.3 cm^{-1}, are only observed under XX configuration. We assign $\sim$140.0 cm^{-1} and $\sim$474.3 cm^{-1} as A_{1g}^2 ($\sim$140.0 cm^{-1}) and A_{1g}^1 ($\sim$474.3 cm^{-1}), respectively.[65] The asymmetric mode $\sim$113.0 cm^{-1} needs further clarification. The E_{2g}^4 mode in CuS$_{1-x}$Se$_x$ (0 < x < 1) had shown the soft mode behavior with decreasing temperature from 300 K to 80 K, which was attributed to the structure phase transition.[64]

The basic structure of SnSe$_2$ (or SnS$_2$) is a trilayer that the Sn layer is sandwiched between two atomic layers of Se (S) atoms. The different stackings of these trilayers will produce possible polytypes including 2H (one trilayer), 4H (two trilayerrs) and 6H (three trilayers). 6H polytype further includes two types, 6Ha and 6Hb.[24] These polytypes exhibit different symmetries, D_{3d} for both 2H and 6Hb, C_{6v} for 4H and C_{3v} for 6Ha. Based on the present Raman spectrum, SnSe$_2$ here is actually 6Hb-SnSe$_2$.[24] Its 27 normal modes are represented by:[24] $\Gamma= 4A_{1g} + 5A_{2u} + 4E_g + 5E_{2u}$, where $4A_{1g}$ and $4E_g$ are Raman active. $2A_{1g}$ (35.5 cm^{-1} and 184.5 cm^{-1}) and $2E_g$ (20.5 cm^{-1} and 109.0 cm^{-1}) have been assigned by Smith $et~al.$.[24] In our Raman spectrum, the four modes lie at $\sim$19.7 cm^{-1}(E_g^2), $\sim$34.4 cm^{-1}(A_{1g}^2), $\sim$109.0 cm^{-1}(E_g^1) and $\sim$182.3 cm^{-1}(A_{1g}^1), respectively. In addition, we observed several weak modes, $\sim$70.9 cm^{-1}, $\sim$147.2 cm^{-1}, $\sim$217.9 cm^{-1} (detected by 633-nm excitation. See Fig. S2 in ESI†), $\sim$251.0 cm^{-1} (detected by 633-nm excitation. See Fig. S2 in ESI†) and $\sim$340.1 cm^{-1}. Two modes, $\sim$70.9 cm^{-1} and $\sim$340.1 cm^{-1}, can be assigned to A_{1g}, while the mode at $\sim$147.2 cm^{-1}

can be assigned to E_g. The other two modes, $\sim$217.9 cm^{-1} and $\sim$251.0 cm^{-1}, are much broad in width, which probably comes from the phonons away from Γ point.

GeSe, GeS, SnS and SnSe belong to D_{2h} with 8 atoms in unit cell forming two tetralayers. 24 normal vibration modes of GeSe are expected and denoted as follows: $\Gamma= 4A_g + 4B_{1u} + 2B_{1g} + 2A_u + 4B_{2g} + 4B_{3u} + 2B_{3g} + 2B_{2u}$, where $4A_g$, $2B_{1g}$, $4B_{2g}$ and $2B_{3g}$ are Raman active.[34] Its Raman modes have been assigned in Section 2:[34] A_g^4 ($\sim$40 cm^{-1}), A_g^3 ($\sim$82 cm^{-1}), A_g^2 ($\sim$175 cm^{-1}) and A_g^1 ($\sim$188 cm^{-1}), B_{3g}^2 ($\sim$39 cm^{-1}) and B_{3g}^1 ($\sim$151 cm^{-1}). A_g^3 ($\sim$40 cm^{-1}) and B_{3g}^2 ($\sim$39 cm^{-1}) are identified as the interlayer shear modes within bc plane.[34]

GaTe belongs to C_{2h}.[66] Its 36 normal vibration modes are represented by $\Gamma= 12A_g + 6B_g + 6A_u + 12B_u$, where $12A_g$ and $6B_g$ modes are Raman active, thus 18 Raman modes are expected.[66] Based on the Raman tensors of A_g and B_g,[29] 10 Raman modes are assigned as follows, A_g ($\sim$40.5 cm^{-1}, $\sim$52.1 cm^{-1}, $\sim$66.2 cm^{-1}, $\sim$109.4 cm^{-1}, $\sim$114.6 cm^{-1}, $\sim$176 cm^{-1}, $\sim$207.7 cm^{-1} and $\sim$268.5 cm^{-1}) and B_g ($\sim$56.3 cm^{-1} and $\sim$162.6 cm^{-1}).[66,67]

ReSe$_2$ has C_i symmetry,[68] whose 36 normal vibration modes are represented by $\Gamma= 18A_g + 18A_u$, where $18A_g$ modes are Raman active. Thus, all the vibration modes in its Raman spectrum are denoted by A_g. These modes lie at $\sim$112.1 cm^{-1}, $\sim$118.3 cm^{-1}, $\sim$121.4 cm^{-1}, $\sim$124.5 cm^{-1}, $\sim$159.6 cm^{-1}, $\sim$172.5 cm^{-1}, $\sim$117.1 cm^{-1}, $\sim$180.7 cm^{-1}, $\sim$192.0 cm^{-1}, $\sim$196.1 cm^{-1}, $\sim$209.9 cm^{-1}, $\sim$218.6 cm^{-1}, $\sim$232.5 cm^{-1}, $\sim$240.0 cm^{-1}, $\sim$248.1 cm^{-1} and $\sim$260.8 cm^{-1}.
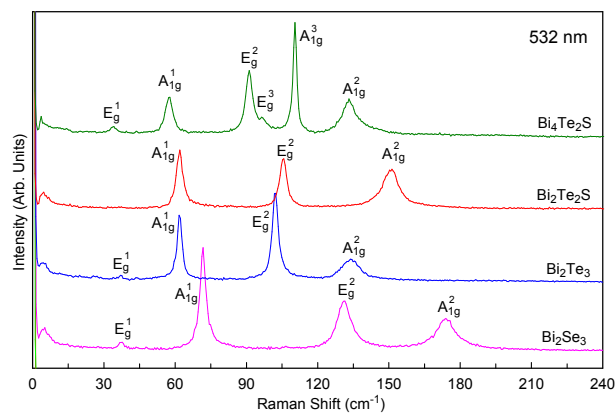
Fig. 4 Raman spectra of Bi$_2$Se$_3$, Bi$_2$Te$_3$, Bi$_2$Te$_2$S and Bi$_4$Te$_2$S.

3.2 Topological insulators

Bi$_2$Se$_3$ and Bi$_2$Te$_3$ have D_{3h} symmetry.[69] Their quintuple layer is in the sequences of Se1(Te1)-Bi-Se2(Te2)-Bi-Se1(Te1). 15 normal vibration modes are represented by $\Gamma= 2E_g + 2A_{1g} + 3E_u + 3A_{1u}$, where $2E_g$ and $2A_{1g}$ modes

are Raman active.[69] Four modes in Bi_2Se_3 and Bi_2Te_3 have been detected and assigned.[33,70] These modes are assigned as follows (Fig. 4), Bi_2Se_3: E_g^1 ($\sim$37.1 cm^{-1}), A_{1g}^1 ($\sim$71.6 cm^{-1}), E_g^2($\sim$130.8 cm^{-1}) and A_{1g}^2 ($\sim$173.6 cm^{-1}); Bi_2Te_3: E_g^1 ($\sim$37.1 cm^{-1}), A_{1g}^1 ($\sim$61.6 cm^{-1}), E_g^2 ($\sim$102.3 cm^{-1}) and A_{1g}^2 ($\sim$133.9 cm^{-1}). When Te2 atomic layer of quintuple layer (Te1-Bi-Te2-Bi-Te1) is replaced by a S atomic layer, Bi_2Te_3 will change into Bi_2Te_2S (Te1-Bi-S-Bi-Te1). Bi_2Te_2S also has D_{3h} symmetry. These modes are found E_g^1 ($\sim$34.9 cm^{-1}) (detected by 633-nm excitation. See Fig. S1 in ESI†), A_{1g}^1 ($\sim$61.6 cm^{-1}), E_g^2($\sim$105.4 cm^{-1}) and A_{1g}^2 ($\sim$150.9 cm^{-1}). When extra Bi bilayer between interlayer Te1-Te1 space is included, Bi_2Te_2S will further change into Bi_4Te_2S (Bi-Bi-Te1-Bi-S-Bi-Te1). There are six modes in the Raman spectrum of Bi_4Te_2S, $\sim$33.7 cm^{-1}, $\sim$90.7 cm^{-1}, $\sim$96.4 cm^{-1} (XX, YX) and $\sim$57.3 cm^{-1}, $\sim$110.4 cm^{-1}, $\sim$133.2 cm^{-1} (XX). We assign these modes as follows: E_{1g}^1 ($\sim$33.7 cm^{-1}), E_{1g}^2 ($\sim$90.7 cm^{-1}), E_{1g}^3 ($\sim$96.4 cm^{-1}), A_{1g}^1 ($\sim$57.3 cm^{-1}), A_{1g}^3 ($\sim$110.4 cm^{-1}) and A_{1g}^2 ($\sim$133.2 cm^{-1}).

3.3 Superconductors, semi-metal and insulators

$NbSe_2$ is a superconductor.[71] It belongs to D_{6h} with two tri-layers in its unit cell. 18 normal vibrational modes are represented by: $\Gamma = 2A_{2u} + 2B_{2g} + B_{1u} + A_{1g} + 2E_{1u} + 2E_{2g} + E_{2u} + E_{1g}$, where A_{1g}, E_{1g} and $2E_{2g}$ modes are Raman active.[72] These modes were found at 228 cm^{-1} (A_{1g}), 133.7 cm^{-1} (E_{1g}), 237 cm^{-1} (E_{2g}^1) and 29.1 cm^{-1} (E_{2g}^2).[72] E_{2g}^2, A_{1g} and E_{2g}^1 in our experiment are found at $\sim$28.4 cm^{-1} (E_{2g}^2), $\sim$228.7 cm^{-1} (A_{1g}) and $\sim$237.5 cm^{-1} (E_{2g}^2), as shown in Fig. 5. Unexpectedly, E_{2g}^1 ($\sim$237.5 cm^{-1}) is only observed by 532-nm excitation, which needs multi-wavelengths excitations for further clarification. In addition, we observed three broad modes, $\sim$95.3 cm^{-1}, $\sim$182.6 cm^{-1} and $\sim$333.5 cm^{-1}. The broad mode $\sim$182.6 cm^{-1} is assigned as a soft mode, which involves a second-order scattering process of two phonons.[72–74] Recently, Xi et al. obtained the charge-density-wave (CDW) transition temperature (33.5 K in bulk $NbSe_2$) by measuring the dependency of this soft mode on the temperature.[75] The other two broad modes need further clarifications.

Graphite belongs to D_{6h} with 12 normal vibrational modes represented by: $\Gamma = 2A_{2u} + 2B_{2g} + 2E_{1u} + 2E_{2g}$, where $2E_{2g}$ modes are Raman active.[21] $2E_{2g}$ modes are found $\sim$43.5 cm^{-1} (E_{2g}^2) and $\sim$1581.3 cm^{-1} (E_{2g}^1, usually called as G mode). Because of the distinctive band structure of graphite, the phonons from K point can also participate in the Raman process. For example, the G' mode (or the so-called 2D mode) that comes from TO phonon close to K point is found at $\sim$2688 cm^{-1} by 633-nm excitation and at $\sim$2720.8 cm^{-1} by 532-nm excitation.[76,77] The dependence of the G' peak position on the laser

wavelength reflects the high dispersive behavior of TO branch around K point.[78,79] Please refer to the comprehensive review articles for the advances on Raman spectroscopy of graphite and graphene.[27,80,81]

BN is an insulator, which is normally used as substrate to support high-quality graphene flakes.[82] It has a similar crystal structure to graphite, in which two carbon atoms in unit cell are replaced by B and N, respectively. Thus, its lattice vibrations at Γ point are similar to those of graphite. E_{2g}^2 and E_{2g}^1 in BN lies at $\sim$52.2 cm^{-1} and $\sim$1364.7 cm^{-1}.[83]

The frequencies and corresponding assignments of these Raman modes are summarized in Table 1. Although we remeasured the Raman spectra of various LMs, there are still a large number of LMs waiting for revisits, which require extensive researches from 2D community. For the convenience of the subsequent researches, in Table 1, we summarized the Raman modes of other 25 LMs reported in literature.

4 Interlayer shear and layer-breathing vibrations

The unit cell of bulk LMs is composed of several rigid layers (RLs) which can be peeled by mechanical exfoliation from bulk materials. For example, there are one RL in $ReSe_2$, Bi_2Se_3 and Bi_2Te_3, and two RLs in graphite, TMDs, GaSe(S), $SnSe_2$, BP, GeSe, BN and $NbSe_2$. The RLs are single atomic layer (monolayer) for graphite and BN, three atomic layer (trilayer) for TMDs, $SnSe_2$ and $NbSe_2$, four atomic layer (tetralayer) for GaSe(S), BP and GeSe, and five atomic layer (quintuple layer) for Bi_2Se_3 and Bi_2Te_3. The stacking of these RLs will form the multilayer structure whose thickness (or layer number) is represented by the number of RLs. The atomic layers in each RL are covalently bonded to one another while the adjacent RLs are coupled via weak van der Waals interactions. There exist two types of distinct Raman modes resulting from the relative vibrations between RLs, the shear (C) and layer breathing (LB) modes, which are due to relative motions of the planes of RLs, either perpendicular or parallel to their normal. The shear mode is referred as the C mode because it was first observed in multilayer graphene (MLG) and provides a direct measurement of the interlayer *coupling*.[21] No C or LB modes are expected in bulk LMs which have only one RL in its unit cell (for example, $ReSe_2$ and Bi_2Se_3).

Only the C modes were observed in Bernal-stacked MLGs, where the C modes were found to decrease in frequency with decreasing layer numbers.[21] The C mode has been used to identify the layer number and probe ultralow-energy electronic excitations in MLGs.[21] However, no LB modes were detected in Bernal-stacked MLG. Both the interlayer C and LB modes were detected in multilayer TMDs.[20,30,98] The investigations of C and LB modes now start to expand to LMs

Table 1 The frequencies and corresponding assignments of different types of LMs.

Crystal	Symmetry	Assignments of the vibrational modes (cm^{-1})
MoS$_2$	D_{6h}	32.5(E_{2g}^2) 383.3(E_{2g}^1) 408.6(A_{1g}) 452.0(2LA(M))
MoSe$_2$	D_{6h}	25.5(E_{2g}^2) 240.6(A_{1g}) 250.5 285.0(E_{2g}^1)
WS$_2$	D_{6h}	27.5(E_{2g}^2) 174(LA(M)) 193 231(A_{1g}(M)) 297(2LA(M)-2E_{2g}^2(M)) 313 324 351.4(2LA(M)) 356.5(E_{2g}^1) 420.0(A_{1g})
WSe$_2$	D_{6h}	23.8(E_{2g}^2) 138 248(E_{2g}^1) 251(A_{1g})^a 258(2LA(M)) 307 359 372 394
GaSe	D_{6h}	19.3(E_{2g}^2) 59.2(E_{1g}^2) 134.0(A_{1g}^2) 209.3(E_{1g}^1)^a 212.6(E_{2g}^1) 307.5(A_{1g}^1)
GaS	D_{6h}	22.4(E_{2g}^2) 74.8(E_{1g}^2) 188.5(A_{1g}^2) 291.2(E_{1g}^1) 295.3(E_{2g}^2) 361.1(A_{1g}^2)
CuS	D_{6h}	19.3(E_{2g}^4) 61.8(E_{2g}^3) 65.0(E_{2g}^2)^a 113.0 140.0(A_{1g}^2) 266.3(E_{2g}^2) 474.3(A_{1g}^1)
6H-SnSe$_2$	D_{3d}	19.7(E_g^2) 34.4(A_{1g}^2) 70.9(A_g^3) 109.0(E_g^1) 147.2(E_g^3) 182.3(A_{1g}^1) 340.1(A_{1g}^4)
GeSe	D_{2h}	39(B_{3g}^2) 40(A_g^4) 82(A_g^3) 151(B_{3g}^1) 175(A_g^2)^a 188(A_g^1)
GaTe	C_{2h}	40.5(A_g) 52.1(A_g) 56.3(B_g) 66.2(A_g) 109.4(A_g) 114.6(A_g) 162.6(B_g) 176.0(A_g) 207.7(A_g) 268.5(A_g)
ReSe$_2$^{b}	C_i	112.1 118.3 121.4 124.5 159.6 172.5 177.1 180.7 192.0 196.1 209.9 218.6 232.5 240.0 248.1 260.8
Bi$_2$Se$_3$	D_{3d}	37.1(E_g^1) 71.6(A_{1g}^1) 130.8(E_g^2) 173.6(A_{1g}^2)
Bi$_2$Te$_3$	D_{3d}	37.1(E_g^1) 61.6(A_{1g}^1) 102.3(E_g^2) 133.9(A_{1g}^2)
Bi$_2$Te$_2$S	D_{3d}	34.9(E_g^1)^a 61.6(A_{1g}^1) 105.4(E_g^2) 150.9(A_{1g}^2)
Bi$_4$Te$_2$S	D_{3d}	33.7(E_g^1) 57.3(A_{1g}^1) 90.7(E_g^2) 96.4(E_g^3) 110.4(A_{1g}^3) 133.2(A_{1g}^2)
Graphite	D_{6h}	43.5(E_{2g}^2) 1581.3(E_{2g}^1) 2676.5^c 2720.8^c
BN	D_{6h}	52.2(E_{2g}^2) 1364.7(E_{2g}^1)
NbSe$_2$	D_{6h}	28.4(E_{2g}^2) 95.3 182.6 228.7(A_{1g}^1) 237.5(E_{2g}^1) 333.5
MoTe$_2$^{d}	D_{6h}	27.5(E_{2g}^2) 116.8(E_{1g}) 174.0(A_{1g}) 234.0(E_{2g}^1)
WTe$_2$^{e,f}	C_{2v}	78.9 88.4 109.9 114.6 129.9 160.6 207.7
BP^g	D_{2h}	197(B_{1g}^1) 233(B_{3g}^1) 365(A_g^1) 440(B_{3g}^2) 442(B_{2g}) 470(A_g^2)
ReS$_2$^{b,h}	C_i	140.3 145.9 153.1 163.6 217.2 237.1 278.3 284.2 307.8 311.0 320.6 324.9 348.8 368.9 377.9 407.3 418.7 438.0
2H-SnS$_2$^{i}	D_{3d}	205.5(E_g) 315.0(A_{1g})
4H-SnS$_2$^{i}	C_{6v}	28.5(E) 200.0(E) 214.0(E) 313.5(A_1)
SnS^j	D_{2h}	40(A_g) 49(B_{3g}) 70(B_{2g}) 85(B_{2g}) 95(A_g) 164(B_{3g}) 192(A_g) 208(B_{1g}) 218(A_g) 290(B_{2g})
SnSe^j	D_{2h}	33(A_g) 37(B_{3g}) 57(B_{1g}) 71(A_g) 108(B_{3g}) 130(A_g) 133(B_{1g}) 151(A_g)
ZrS$_2$^{l}	D_{3d}	251(E_g) 316(A_{2u}(LO)) 333(A_{1g}) 350(E_u(LO)) 700(2E_u(LO))
ZrTe$_2$^{k}	D_{3d}	104(E_g) 145(A_{1g})
CoS$_2$^{m}	T_h	289(E_g) 316(T_g^1) 392(A_g) 416(T_g^2)
CoSe$_2$^{n}	T_h	188(A_g)
HfS$_2$^{o}	D_{3d}	260(E_g) 321(E_u(LO)) 337(A_{1g})
HfSe$_2$^{o}	D_{3d}	96(E_u(TO)) 120(A_{2u}(TO)) 145(E_g) 170(A_{2u}(LO)) 198(A_{1g}) 210(E_u(LO))
HfTe$_2$^{k}	D_{3d}	107(E_g) 149(A_{1g})
TiS$_2$^{p}	D_{3d}	232(E_g) 336(A_{1g})
TiSe$_2$^{q}	D_{3d}	136(E_g) 200(A_{1g})
TiTe$_2$^{k}	D_{3d}	102(E_g) 145(A_{1g})
1T-TaS$_2$^{r}	D_{3d}	240(E_g) 385(A_{1g})
1T-TaSe$_2$^{s}	D_{3d}	23(E_{2g}^2) 139(E_{1g}) 207(E_{2g}^1) 234(A_{1g})
2H-TaS$_2$^{k,t}	D_{6h}	26(E_{2g}^2) 230(E_{1g}) 285(E_{2g}^1) 400(A_{1g})
2H-TaSe$_2$^{t}	D_{6h}	23(E_{2g}^2) 139(E_{1g}) 207(E_{2g}^1) 234(A_{1g})
NbS$_2$^{t}	D_{6h}	31(E_{2g}^2) 260(E_{1g}) 304(E_{2g}^1) 379(A_{1g})
FeSe^u	D_{6h}	106(E_g) 160(A_{1g}) 224(B_{1g}) 234(E_g) 254

^{a} detected by 633-nm excitation; ^{b} all the modes belong to A_g; ^{c} the so-called G′ or 2D mode; ^{d} ref. 84; ^{e} ref. 85; ^{f} all the modes belong to A; ^{g} ref. 42; ^{h} ref. 86; ^{i} ref. 24; ^{j} ref. 40; ^{k} ref. 87; ^{l} ref. 88; ^{m} ref. 89; ^{n} ref. 90; ^{o} ref. 91; ^{p} ref. 92; ^{q} ref. 93; ^{r} ref. 94; ^{s} ref. 95; ^{t} ref. 96; ^{u} ref. 97, measured at 3K.
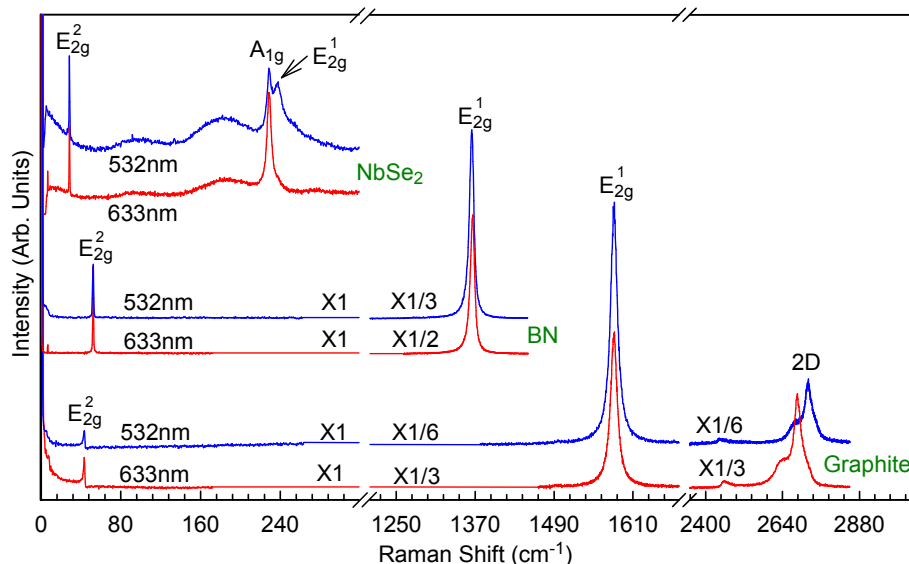
Fig. 5 Raman spectra of NbSe$_2$, Graphite and BN under the 633-nm and 532-nm excitations.

with low symmetries, such as BP and ReSe$_2$.[99–102] However, the C and LB modes are only revealed in several LMs, there are various LMs waiting for explorations.

Next, we first review the main results of linear chain model (LCM), which can predict the frequency of the C and LB modes of multilayer LMs from that of the bulk ones. Then we apply it to different bulk LMs from which we obtain their shear modulus. Finally, we review the recent works about the role of layer stacking configurations on the intensities of C and LB vibrations. The applications of interlayer vibrations to identify the layer number and to probe interlayer coupling of multilayer LMs can be found in the previous review paper.[10]

4.1 Linea chain model for interlayer vibrations

For the C and LB modes, each RL vibrates as a unit and the relative displacements between atoms within RL can be ignored. Therefore, an entire RL can be treated as a single ball once one simulates the C and LB modes in multilayer LMs. Based on this assumption, Zhang *et al.* built a linear chain model (LCM) and successfully produced the frequency trends of both C and LB modes on layer numbers of multilayer MoS$_2$.[20] LCM has been expended to general LMs,[10,103] 2D heterostructures[13,15,104] and 2D alloys.[19]

For in-plane isotropic multilayer LMs, the C mode is doubly degenerate. For an N layer (NL-) LM, there are N-1 pairs of C modes and N-1 LB modes. We denote each C and LB mode of the NL-LM as $C_{N,N-j}$ and $LB_{N,N-j}$, respectively, where N is the layer number, j is phonon branches and $j=N$-1, N-2, ..., 2, 1. If one only consider the nearest-neighbor interlayer interactions in the NL-LM, the corresponding dynamic matrix

can be built up.[13] By solving the dynamic matrix, the frequencies of the $C_{N,N-j}$ and $LB_{N,N-j}$ modes in the NL-LM can be, respectively, expressed by

$$\omega(C_{N,N-j}) = \omega(C_{bulk})sin(j\pi/2N) \qquad (2)$$

and

$$\omega(LB_{N,N-j}) = \omega(LB_{bulk})sin(j\pi/2N), \qquad (3)$$

where $\omega(C_{bulk}) = (1/\pi c)\sqrt{\alpha^{\parallel}/\mu}$ and $\omega(LB_{bulk}) = (1/\pi c)\sqrt{\alpha^{\perp}/\mu}$, c is the speed of light, $\alpha^{\parallel}$ ($\alpha^{\perp}$) is the interlayer force constant per unit area between two RLs of the LM within the basal plane (along c axis), μ is the total mass per unit area in each RL of the LM. Based on equations (2) and (3), $C_{N,1}$ ($LB_{N,1}$) is the highest-frequency C (LB) mode while $C_{N,N-1}$ ($LB_{N,N-1}$) is the lowest one for N layer LM. Fig. 6a shows the branches ($j = N-1, N-2, ...$) for the C modes and Fig. 6b shows the branches ($j = 1, 2, ...$) for the LB modes. In Fig. 6, it is found that once $\omega(C_{bulk})$ and $\omega(LB_{bulk})$ are normalized to $\sqrt{2}$, the frequency of the C and LB modes of the bilayer LM is equal to 1, i.e., $\omega(C_{21})=\omega(LB_{21})=1$.

The normalized experimental frequencies[20] of the C and LB modes in multilayer MoS$_2$ by the corresponding $\omega(C_{21})$ and $\omega(LB_{21})$ are included in the squares in Fig. 6(a) and circles in Fig. 6(b), respectively. The experimental data can be well modeled by the LCM, indicating that the interaction between LM flakes and substrate can be neglected. One can see that the observed C modes in multilayer MoS$_2$ mainly come from the branches ($j = N-1, N-3$ and $N-5$) whose frequency increases with increasing N, while the observed LB modes mainly come from the branches ($j = 1, 3, 5$) whose
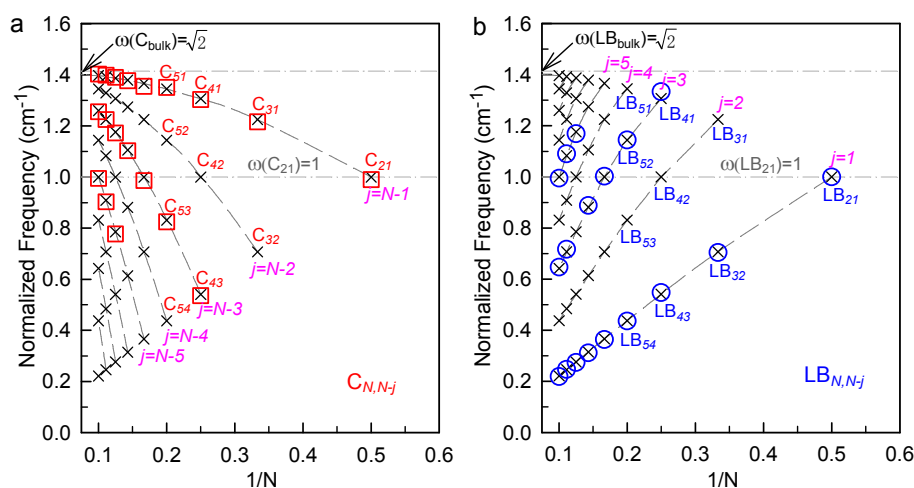
Fig. 6 The frequency of the interlayer C (a) and LB (b) modes in multilayer LMs as a function of inverse layer number (N), where $\omega(C_{21})$ and $\omega(LB_{21})$ are normalized to 1. The squares in (a) and circles in (b) are the normalized experimental frequencies of the C and LB modes in multilayer MoS_2 by the corresponding $\omega(C_{21})$ and $\omega(LB_{21})$, respectively.

frequency decreases with increasing N. However, in Bernal-stacked multilayer graphenes,[21] only the $j = N-1$ branch is detected for the C modes. The LCM of equations (2) and (3) describes a robust link between $\omega(C_{N,N-j})$ ($\omega(LB_{N,N-j})$) and the corresponding frequency in bulk LMs. Once $\omega(C_{bulk})$ or $\omega(LB_{bulk})$ is measured for a specific LM, one can obtain the frequency of the C and LB modes in NL-LMs. This affords a fast method to characterize the flake thickness of multilayer LMs, as done for the flakes of 2D alloy.[19]

4.2 Shear modulus

We now apply the LCM to the studied LMs. We mainly focus on the C modes of bulk LMs because they are usually Raman active. From $\omega(C_{bulk})$, we can obtain $\alpha^{\parallel}$ in bulk LMs. For MoS_2, $\omega(C_{bulk}) \sim 32.5$ cm^{-1}, $\mu = 3.0 \times 10^{-7}$ g/cm^2, and we can obtain $\alpha^{\parallel} = 2.82 \times 10^{19}$ N/m^3. $\alpha^{\parallel}$ times the interlayer distance (d) gives the shear modulus of ~ 18.9 GPa for bulk MoS_2.[20] For graphite, $\omega(C_{bulk}) \sim 43.5$ cm^{-1}, $\mu = 7.6 \times 10^{-8}$ g/cm^2, we have $\alpha^{\parallel} = 1.28 \times 10^{19}$ N/m^3 and shear modulus is ~ 4.3 GPa.[21] Thus, one can easily obtain the shear modulus for each bulk LM once its $\omega(C_{bulk})$ is detected by the ultralow-frequency technique.[21] In-plane lattice constant(a), interlayer distance(d), $\omega_C(bulk)$, interlayer forces constant per unit area ($\alpha^{\parallel}$), shear modulus of various LMs and their corresponding references are summarized in Table 2. Here a and d are obtained from Inorganic Crystal Structure Database (ICSD). It should be noted that D_{2h} of bulk GeSe breaks the degenerate C modes within bc plane and gives two C modes for bulk GeSe, i.e., ~ 40 cm^{-1} along c axis and ~ 39 cm^{-1} along b axis. Thus, we have two interlayer force constant and two corresponding shear modulus (Table 2). In the case of 6Hb-SnSe$_2$,

2 C modes are $E_g + E_u$. The E_g mode is observed ~ 19.7 cm^{-1}. Interpretation of interlayer force constant of 6Hb-SnSe$_2$ needs more works on the observation of the E_u mode or the E_g mode in few-layer 6Hb-SnSe$_2$. The shear modulus obtained here are in good agreement with the reported experimental value for MoS_2 and $NbSe_2$,[105] for GaS and GaSe,[106] and for graphite.[107] $\omega(C_{bulk})$ in graphite and BN are relative higher than other materials, however, small in-plane lattice constants and interlayer distance results in the smaller interlayer force constant and shear modulus. Shear modulus reflects the deformation of LMs when they are applied by external strain parallel to the layer plane, which leads to the modifications of electrical and phonon structures for LMs.[108–110]

4.3 Stacking-configuration dependent interlayer mode intensity

Different types of layer stacking configurations are found in LMs. For example, there are two types of layer stacking in multilayer graphene, Bernal (AB) and Rhombohedral (ABC) stackings. In bulk and synthesized multilayer MX$_2$ TMDs, in addition to the most stable, dominant and natural 2H stacking pattern (Fig. 7a), 3R stacking (Fig. 7b) also exists.[111–113] It should be pointed out that 2H and 3R of MX$_2$ are actually much similar to AB and ABC stacking of graphene, respectively. Moreover, one can re-stack the synthesized monolayers to create twisted multilayers (characterized by the mutual rotation angle θ) with new properties.[13,15,114,115] Actually, $\theta = 60°$ corresponds to 2H stacking, while $\theta = 0°$ is 3R stacking. The re-stacking of monolayers obtained from different LMs is considered as a potential tool to create artificially vdWHs for electronic and optoelectronic applications.

Table 2 In-plane lattice constant (a), interlayer distance (d), $\omega(C_{bulk})$, interlayer forces constant per unit area ($\alpha^{\parallel}$), shear modulus (C_{44}) determined by the C mode frequency and that (C_{44}^{*}) obtained by other methods.

Crystal	a (10^{-8}cm)	d (10^{-8}cm)	$\omega_C(bulk)$ (cm^{-1})	$\alpha^{\parallel}$ (10^{19}N/m^3)	C_{44} (GPa)	C_{44}^{*}(GPa)
MoS$_2$	3.15	6.15	32.5	2.82	18.9	18.6[a]
MoSe$_2$	3.29	6.46	25.5	2.60	16.8	
WS$_2$	3.18	6.25	27.5	3.16	19.7	
WSe$_2$	3.28	6.48	23.8	3.06	19.8	
GaSe	3.75	7.96	19.3	1.44	11.5	9.0$\pm$1[b]
GaS	3.59	7.75	22.4	1.38	10.6	9.96$\pm$0.15[b]
CuS	3.79	8.17	19.3	1.73	14.2	
Graphite	2.46	3.35	43.5	1.28	04.3	4.6[c]
BN	2.50	3.33	52.2	1.83	06.1	
NbSe$_2$	3.44	6.27	28.4	2.92	18.3	19.0[a]
GeSe	4.38[d]	5.41	40.0[f]	4.26	23.1	
GeSe	3.83[e]	5.41	39.0[g]	4.05	21.9	

[a] ref. 105; [b] ref. 106; [c] ref. 107; [d] c = 4.38; [e] b = 3.83; [f] along c axis; [g] along b axis.

The intensity of C (LB) mode is found strongly dependent on layer stacking configurations. Zhang *et al.* found that the highest-frequency C modes ($C_{N,1}$) which have been detected in multilayer graphenes with AB stacking totally disappear in ones with ABC stacking at room temperature.[21,103] The lowest-frequency C mode ($C_{N,N-1}$) is not observed in AB stacked trilayer graphene,[21] but detected by Lui *et al.* in ABC stacked by suspending the sample and increasing the laser power up to $\sim$ 9 mW.[117] Puretzky *et al.* found that the intensity of C modes ($C_{N,1}$) in bilayer MoSe$_2$ with 3R stacking drops by a factor of 3.9 compared to 2H stacking, which is accompanied by a redshift of 0.4 cm^{-1} (Fig. 7c).[111] Similar drops in intensity are further revealed in multilayer structures.[111,113] The much differences in intensity serve as fingerprints to characterize layer stacking configurations. Recently, Luo *et al.* proposed a general bond polarizability model to calculate the intensity of C modes in LMs with different stacking configurations.[118] They found that the change in polarizability is maximized for the lowest-frequency C mode ($C_{N,N-1}$) in ABC stacked materials, but not for the highest-frequency C mode ($C_{N,1}$) in AB stacked materials, regardless of the details of the space group.[118] Here, we can see that interlayer vibrations can be used to characterize not only the layer numbers, but also layer stacking configurations.

5 In-plane anisotropic LMs

Many LMs with the high symmetry (D_{6h}), such as graphite and TMDs, have been under intensive investigations.[8,10,26,27,81] The properties of these LMs are isotropic with *ab* plane because of D_{6h} symmetry. Other LMs who have lower symmetry, such as BP (D_{2h}) and ReSe$_2$ (C_i) now start to receive extensive researches.[100,111,119] BP is a narrow gap (0.3 eV in bulk) semiconductor which bridges the space

between zero-gap graphene and large-gap TMDs. Thin film BP has a much high Hall mobility $\sim$1000 cm^{2}V^{-1}s^{-1} which is predicted up to $\sim$10,000 cm^{2}V^{-1}s^{-1} in monolayer.[120,121] As manifested by its optical conductivity and Hall mobility, BP has much strong in-plane anisotropy.[119] This in-plane anisotropy actually comes from the nature of D_{2h}. Thus, GeSe(S) and SnSe(S) should have similar in-plane anisotropy. The nature anisotropy within the layer plane is potential for polarizers, polarization sensor, plasmonic devices and high-performance transistors.[119,122,123]

The in-plane anisotropic properties in ReSe$_2$ can be revealed by optical transmission and reflection normal to the layer plane, and by Raman scattering.[86,100,124–127] Recent advances on these low-symmetry LMs prove that Raman spectroscopy has potentials in revealing the in-plane anisotropy, especially on the polarization-resolved and ultralow-frequency Raman spectroscopies. For example, in an anisotropic LM, the C modes are non-degenerated and each pair of the C modes should be denoted as C^x and C^y. The LCM can also be applied to the non-degenerated C modes, and the frequencies of the $C^x_{N,N-j}$ and $C^y_{N,N-j}$ modes can be also expressed by the equation (2).

Here, we focus on the review of Raman spectroscopy to characterize the in-plane anisotropy in BP and ReSe$_2$. The polarization-resolved Raman spectra of a BP thin film at high frequency region has been obtained.[116,119,128,129] Wang *et al.* found that the peak positions of three modes (A_g^1, B_{2g} and A_g^2) do not change as the excitation light polarization varies (Fig. 8). However, the relative intensities of these three modes change significantly with incident light polarization, which can be used to identify the crystalline orientation of BP thin films. According to the inelastic neutron scattering measurement on bulk BP, there are two C modes around 19 cm^{-1} and 52 cm^{-1}, and one LB mode around 87 cm^{-1}. LB modes in
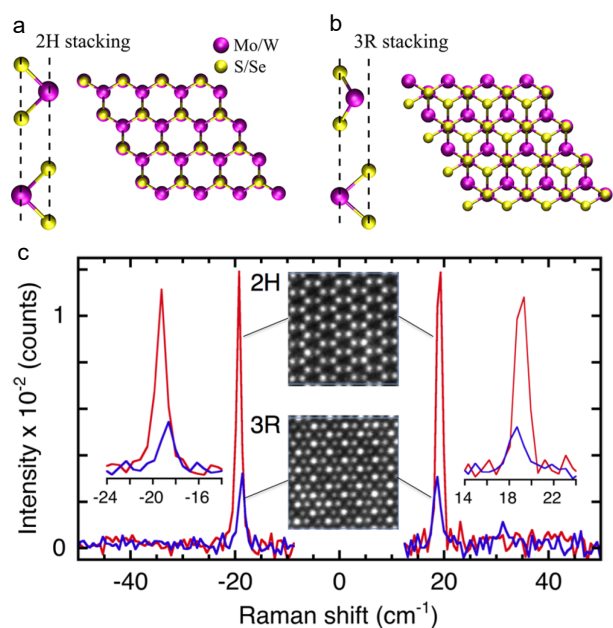
Fig. 7 Side and top views of (a) 2H and (b) 3R stacking patterns of bilayer MX_2. (c) Raman spectra of bilayer $MoSe_2$ for 2H and 3R stacking patterns. Stokes (right) and anti-Stokes (left) low-frequency Raman spectra of $MoSe_2$ bilayers suspended on a TEM grid. The insets show atomic resolution STEM images of the 2H (top) and 3R (bottom) stacking patterns. Reproduced with permission from ref. 111. Copyright 2015, American Chemical Society.
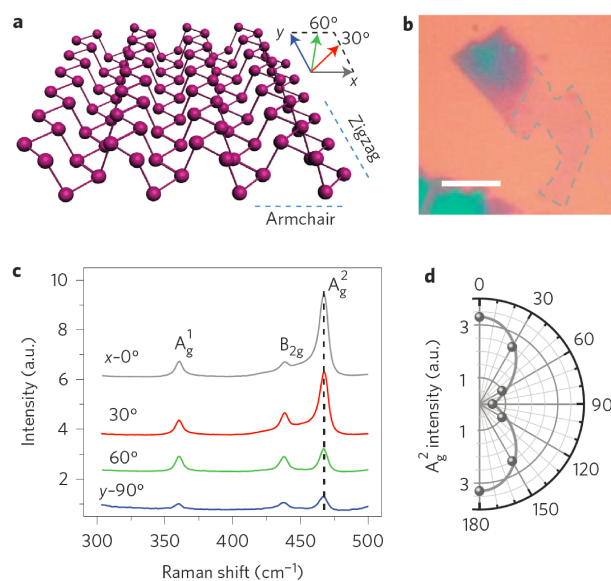

Fig. 8 (a) Schematic of monolayer BP. (b) Optical micrograph of an exfoliated monolayer BP flake on 285 nm SiO_2/Si substrate. (c) Polarization-resolved Raman spectra of monolayer BP with linearly polarized laser excitation. (d) Intensity of the A_g^2 mode as a function of the excitation laser polarization angle in the xy plane. Reproduced with permission from ref. 116. Copyright 2015, Nature Publishing Group.

multilayer BP are recently revealed.[99,130] Ling *et al.* detected three low-frequency modes ($\sim$26.2 cm^{-1}, $\sim$75.6 cm^{-1} and $\sim$85.6 cm^{-1}) in thin BP films. They pointed out that these three modes are the LB modes, and assign them as A_g based on the polarization dependence measurement and theoretical analysis.[99] The dependencies of LB modes on accurate layer numbers are not revealed because of the difficulties in obtaining few-layer BP. Moreover, the experimental works on revealing the C modes in multilayer BP are still lacking.

The polarization-resolved Raman spectra of monolayer, few-layer and bulk $ReSe_2$ are discussed by Wolverson *et al.*.[124] No changes in the frequencies of the Raman bands with layer thickness down to one monolayer are observed, but significant changes in relative intensity of the bands allow the determination of crystal orientation and of monolayer region. As discussed above, there is only on RL in bulk $ReSe_2$ which can not support the interlayer vibration. However, interlayer vibrations in multilayer $ReSe_2$ and ReS_2 were recently revealed by several groups.[100–102,131,132] The emergences of C and LB modes in multilayer structure indicate the non-negligible interlayer coupling and well-defined stacking orders in the $ReSe_2$ and ReS_2 crystals. In particularly, the in-plane anisotropy lifts the degeneracy between C modes

vibrating parallel (C^x) and perpendicular (C^y) to the rhenium chains (b axis).[102,131] Zhao *et al.* predicted and measured two C modes (12.1 cm^{-1} and 13.2 cm^{-1}) and one LB mode (24.8 cm^{-1}) in bilayer $ReSe_2$ (Fig. 9a and Fig. 9b) with a strong angular dependence of the Raman intensity.[100] The frequency between two C modes is only $\sim$1 cm^{-1}. However, a larger frequency difference $\sim$3.5 cm^{-1} between two C modes (13 cm^{-1} and 16.5 cm^{-1}) are revealed in bilayer ReS_2.[102,131] Qiao *et al.* revealed two stable stacking order for N layer ReS_2.[131] They also revealed the unexpected strong interlayer coupling in these two types of ReS_2 whose force constants are 55-99% to those of multilayer MoS_2. The predicted trends of C and LB modes by LCM are observed, which allows the fast layer thickness characterization.[101,102,131,132] The splitting of the in-plane C modes and the strong angular dependence of the Raman intensity of the C and LB modes are the direct fingerprint of the pronounced optical anisotropy in in-plane anisotropic LMs.

6 Conclusion

Lattice vibrations and Raman spectra of bulk LMs is a basic background to explore the layer-dependent phonon properties of multilayer LMs. Here, we first introduce a unified method based on symmetry analysis and polarization Raman
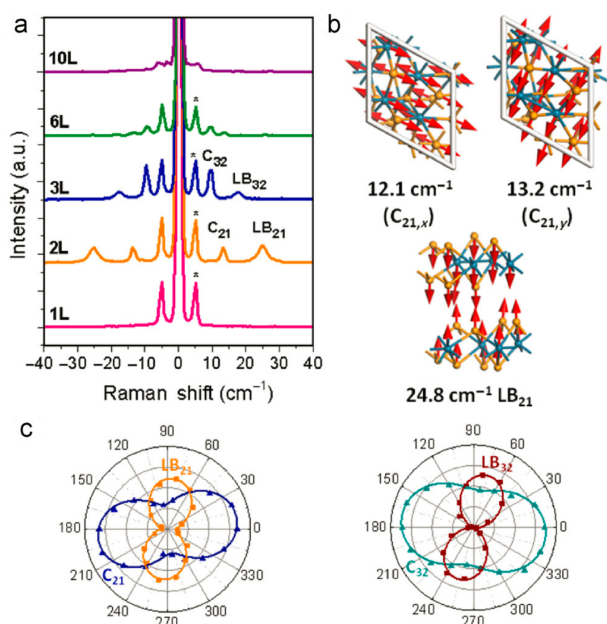
Fig. 9 (a) Raman spectra of few-layer ReSe₂. (b) Schematic of the 3 low frequency vibration modes of bilayer ReSe₂ obtained from first-principle calculations. (c) Polarization resolved Raman peak intensity of bilayer (left panel) and trilayer (right panel) ReSe₂. The dots in both figures represent experimental data, while the lines are theoretical fits from the Raman tensor analysis. Reproduced with permission from ref. 100. Copyright 2015, Royal Society of Chemistry.

References

1 K. S. Novoselov and A. H. C. Neto, *Physica Scripta*, 2012, **2012**, 014006.
2 F. Bonaccorso, A. Lombardo, T. Hasan, Z. Sun, L. Colombo and A. C. Ferrari, *Materials Today*, 2012, **15**, 564 – 589.
3 J. N. Coleman, M. Lotya, A. ONeill, S. D. Bergin, P. J. King, U. Khan, K. Young, A. Gaucher, S. De, R. J. Smith, I. V. Shvets, S. K. Arora, G. Stanton, H.-Y. Kim, K. Lee, G. T. Kim, G. S. Duesberg, T. Hallam, J. J. Boland, J. J. Wang, J. F. Donegan, J. C. Grunlan, G. Moriarty, A. Shmeliov, R. J. Nicholls, J. M. Perkins, E. M. Grieveson, K. Theuwissen, D. W. McComb, P. D. Nellist and V. Nicolosi, *Science*, 2011, **331**, 568–571.
4 K. F. Mak, C. Lee, J. Hone, J. Shan and T. F. Heinz, *Phys. Rev. Lett.*, 2010, **105**, 136805.
5 A. Splendiani, L. Sun, Y. Zhang, T. Li, J. Kim, C.-Y. Chim, G. Galli and F. Wang, *Nano Lett.*, 2010, **10**, 1271–1275.
6 B. Radisavljevic, A. Radenovic, J. Brivio, V. Giacometti and A. Kis, *Nat. Nanotech.*, 2011, **6**, 147–150.
7 Y. Zhang, J. Ye, Y. Matsuhashi and Y. Iwasa, *Nano Lett*, 2012, **12**, 1136–1140.
8 Q. H. Wang, K. Kalantar-Zadeh, A. Kis, J. N. Coleman and M. S. Strano, *Nat. Nanotech.*, 2012, **7**, 699–712.
9 S. Z. Butler, S. M. Hollen, L. Cao, Y. Cui, J. A. Gupta, H. R. Gutirrez, T. F. Heinz, S. S. Hong, J. Huang, A. F. Ismach, E. Johnston-Halperin, M. Kuno, V. V. Plashnitsa, R. D. Robinson, R. S. Ruoff, S. Salahuddin, J. Shan, L. Shi, M. G. Spencer, M. Terrones, W. Windl and J. E. Goldberger, *ACS Nano*, 2013, **7**, 2898–2926.
10 X. Zhang, X.-F. Qiao, W. Shi, J.-B. Wu, D.-S. Jiang and P.-H. Tan, *Chem. Soc. Rev.*, 2015, **44**, 2757–2785.
11 S. Bertolazzi, D. Krasnozhon and A. Kis, *ACS Nano*, 2013, **7**, 3246–3252.
12 K. Kośmider and J. Fernández-Rossier, *Phys. Rev. B*, 2013, **87**, 075451.
13 J.-B. Wu, X. Zhang, M. Ijas, W.-P. Han, X.-F. Qiao, X.-L. Li, D.-S. Jiang, A. C. Ferrari and P.-H. Tan, *Nat Comm.*, 2014, **5**, 5309.
14 F. Withers, O. Del Pozo-Zamudio, A. Mishchenko, A. P. Rooney, A. Gholinia, K. Watanabe, T. Taniguchi, S. J. Haigh, A. K. Geim, A. I. Tartakovskii and K. S. Novoselov, *Nat Mater*, 2015, **14**, 301–306.
15 J.-B. Wu, Z.-X. Hu, X. Zhang, W.-P. Han, Y. Lu, W. Shi, X.-F. Qiao, M. Ijias, S. Milana, W. Ji, A. C. Ferrari and P.-H. Tan, *ACS Nano*, 2015, **9**, 7440–7449.
16 Y. Chen, D. O. Dumcenco, Y. Zhu, X. Zhang, N. Mao, Q. Feng, M. Zhang, J. Zhang, P.-H. Tan, Y.-S. Huang and L. Xie, *Nanoscale*, 2014, **6**, 2833–2839.
17 J. Mann, Q. Ma, P. M. Odenthal, M. Isarraraz, D. Le, E. Preciado, D. Barroso, K. Yamaguchi, G. von Son Palacio, A. Nguyen, T. Tran, M. Wurch, A. Nguyen, V. Klee, S. Bobek, D. Sun, T. F. Heinz, T. S. Rahman, R. Kawakami and L. Bartels, *Adv. Mater.*, 2014, **26**, 1399–1404.
18 Q. Feng, Y. Zhu, J. Hong, M. Zhang, W. Duan, N. Mao, J. Wu, H. Xu, F. Dong, F. Lin, C. Jin, C. Wang, J. Zhang and L. Xie, *Adv. Mater.*, 2014, **26**, 2648–2653.
19 X.-F. Qiao, X.-L. Li, X. Zhang, W. Shi, J.-B. Wu, T. Chen and P.-H. Tan, *Appl. Phys. Lett.*, 2015, **106**, 223102.
20 X. Zhang, W. P. Han, J. B. Wu, S. Milana, Y. Lu, Q. Q. Li, A. C. Ferrari and P. H. Tan, *Phys. Rev. B*, 2013, **87**, 115413.

measurements to assign the observed modes in Raman spectra of bulk LMs. Then, we revisit and update the peak positions and mode assignments of different types of bulk LMs in three sub-sections by re-measuring their Raman spectra. We further apply the recent advances on interlayer vibrations of multi-layer graphene and TMDs to these LMs from which we obtain their shear modulus. The detected C or LB modes in bulk LMs allow to build a robust link between the frequencies of the corresponding modes in multilayer LMs and their layer numbers, which will benefit the future layer thickness characterization of multilayer LMs. We also summaries the role of layer stacking configurations on the intensities of interlayer vibrations. Finally, we review the application of Raman spectroscopy in revealing the in-plane anisotropy by both high-frequency and ultralow-frequency vibrations. We believe that this review will accelerate and benefit the researches on these different types of LMs, particulary when they are reduced or isolated down to monolayer and few layers.

21 P. H. Tan, W. P. Han, W. J. Zhao, Z. H. Wu, K. Chang, H. Wang, Y. F. Wang, N. Bonini, N. Marzari, N. Pugno, G. Savini, A. Lombardo and A. C. Ferrari, *Nat. Mater.*, 2012, **11**, 294–300.

22 J. Irwin, R. Hoff, B. Clayman and R. Bromley, *Solid State Comm.*, 1973, **13**, 1531 – 1536.

23 T. J. Wieting and J. L. Verble, *Phys. Rev. B*, 1972, **5**, 1473–1479.

24 A. J. Smith, P. E. Meek and W. Y. Liang, *J. Phys. C: Solid State Phys.*, 1977, **10**, 1321.

25 K. S. Novoselov, A. K. Geim, S. V. Morozov, D. Jiang, Y. Zhang, S. V. Dubonos, I. V. Grigorieva and A. A. Firsov, *Science*, 2004, **306**, 666–669.

26 K. F. Mak, J. Shan and T. F. Heinz, *Phys. Rev. Lett.*, 2010, **104**, 176404.

27 A. C. Ferrari and D. M. Basko, *Nat. Nanotech.*, 2013, **8**, 235–246.

28 G. Y. Zhang, G. X. Lan and Y. F. Wang, *Lattice Vibration Spectroscopy, 2nd ed.*, High Education Press, China, 1991.

29 R. Loudon, *Adv. Phys*, 2001, **50**, 813–864.

30 Y. Zhao, X. Luo, H. Li, J. Zhang, P. T. Araujo, C. K. Gan, J. Wu, H. Zhang, S. Y. Quek, M. S. Dresselhaus and Q. Xiong, *Nano Lett*, 2013, **13**, 1007–1015.

31 W. Richter and C. R. Becker, *Phys. Status Solidi B*, 1977, **84**, 619–628.

32 H. Zhang, C.-X. Liu, X.-L. Qi, X. Dai, Z. Fang and S.-C. Zhang, *Nat Phys*, 2009, **5**, 438–442.

33 J. Zhang, Z. Peng, A. Soni, Y. Zhao, Y. Xiong, B. Peng, J. Wang, M. S. Dresselhaus and Q. Xiong, *Nano Lett.*, 2011, **11**, 2407–2414.

34 H. Chandrasekhar and U. Zwick, *Solid State Comm.*, 1976, **18**, 1509 – 1513.

35 H. Wiedemeier and H. G. von Schnering, *Zeitschrift fur Kristallographie*, 1978, **148**, 295–303.

36 J. L. Verble and T. J. Wieting, *Phys. Rev. Lett.*, 1970, **25**, 362–365.

37 C. Ataca, M. Topsakal, E. Akturk and S. Ciraci, *J. Phys. Chem. C*, 2011, **115**, 16354–16361.

38 H. Li, Q. Zhang, C. C. R. Yap, B. K. Tay, T. H. T. Edwin, A. Olivier and D. Baillargeat, *Adv. Funct. Mater.*, 2012, **22**, 1385–1390.

39 L. Makinistian and E. A. Albanesi, *J. Phys.: Condens. Matter*, 2007, **19**, 186211.

40 H. R. Chandrasekhar, R. G. Humphreys, U. Zwick and M. Cardona, *Phys. Rev. B*, 1977, **15**, 2177–2183.

41 V. L. Deringer, R. P. Stoffel and R. Dronskowski, *Phys. Rev. B*, 2014, **89**, 094303.

42 S. Sugai and I. Shirotani, *Solid State Comm.*, 1985, **53**, 753 – 755.

43 G.-B. Liu, D. Xiao, Y. Yao, X. Xu and W. Yao, *Chem. Soc. Rev.*, 2015, **44**, 2643–2663.

44 H. Schmidt, F. Giustiniano and G. Eda, *Chem. Soc. Rev.*, 2015, **44**, 7715–7736.

45 X. Duan, C. Wang, A. Pan, R. Yu and X. Duan, *Chem. Soc. Rev.*, 2015, **44**, 8859–8876.

46 D. Voiry, A. Mohite and M. Chhowalla, *Chem. Soc. Rev.*, 2015, **44**, 2702–2712.

47 Y. Chen, C. Tan, H. Zhang and L. Wang, *Chem. Soc. Rev.*, 2015, **44**, 2681–2701.

48 H. Wang, H. Yuan, S. Sae Hong, Y. Li and Y. Cui, *Chem. Soc. Rev.*, 2015, **44**, 2664–2680.

49 Y. Shi, H. Li and L.-J. Li, *Chem. Soc. Rev.*, 2015, **44**, 2744–2756.

50 H. Liu, Y. Du, Y. Deng and P. D. Ye, *Chem. Soc. Rev.*, 2015, **44**, 2732–2743.

51 C. Tan and H. Zhang, *Chem. Soc. Rev.*, 2015, **44**, 2713–2731.

52 H. Zeng and X. Cui, *Chem. Soc. Rev.*, 2015, **44**, 2629–2642.

53 C. Tan, Z. Liu, W. Huang and H. Zhang, *Chem. Soc. Rev.*, 2015, **44**, 2615–2628.

54 A. Kuc and T. Heine, *Chem. Soc. Rev.*, 2015, **44**, 2603–2614.

55 Q. Ji, Y. Zhang, Y. Zhang and Z. Liu, *Chem. Soc. Rev.*, 2015, **44**, 2587–2602.

56 Y. Sun, S. Gao, F. Lei and Y. Xie, *Chem. Soc. Rev.*, 2015, **44**, 623–636.

57 T. Sekine, M. Izumi, T. Nakashizu, K. Uchinokura and E. Matsuura, *J. Phys. Soc. Jpn.*, 1980, **49**, 1069–1077.

58 P. Tonndorf, R. Schmidt, P. Böttger, X. Zhang, J. Börner, A. Liebig, M. Albrecht, C. Kloc, O. Gordan, D. R. T. Zahn, S. M. de Vasconcellos and R. Bratschitsch, *Opt. Express*, 2013, **21**, 4908–4916.

59 W. Zhao, Z. Ghorannevis, K. K. Amara, J. R. Pang, M. Toh, X. Zhang, C. Kloc, P. H. Tan and G. Eda, *Nanoscale*, 2013, **5**, 9677–9683.

60 A. Berkdemir, H. R. Gutirrez, A. R. Botello-Mndez, N. Perea-Lpez, A. L. Elłas, C.-I. Chia, B. Wang, V. H. Crespi, F. Lpez-Urłas, J.-C. Charlier, H. Terrones and M. Terrones, *Sci. Rep.*, 2013, **3**, 1755.

61 J. M. Auerhammer and E. R. Eliel, *Opt. Lett.*, 1996, **21**, 773–775.

62 P. Hu, Z. Wen, L. Wang, P. Tan and K. Xiao, *ACS Nano*, 2012, **6**, 5988–5994.

63 N. Gasanly, A. Aydinli, H. Özkan and C. Kocabas, *Solid State Comm.*, 2000, **116**, 147 – 151.

64 M. Ishii, K. Shibata and H. Nozaki, *J. Solid. State. Chem.*, 1993, **105**, 504 – 511.

65 C. Sourisseau, R. Cavagnat and M. Fouassier, *J. Phys. Chem. Solids*, 1991, **52**, 537 – 544.

66 J. C. Irwin, B. P. Clayman and D. G. Mead, *Phys. Rev. B*, 1979, **19**, 2099–2105.

67 A. Yamamoto, A. Syouji, T. Goto, E. Kulatov, K. Ohno, Y. Kawazoe, K. Uchida and N. Miura, *Phys. Rev. B*, 2001, **64**, 035210.

68 D. Wolverson, S. Crampin, A. S. Kazemi, A. Ilie and S. J. Bending, *ACS Nano*, 2014, **8**, 11154–11164.

69 W. Richter and C. R. Becker, *physica status solidi (b)*, 1977, **84**, 619–628.

70 K. M. F. Shahil, M. Z. Hossain, V. Goyal and A. A. Balandin, *J. Appl. Phys.*, 2012, **111**, 054305.

71 T. Yokoya, T. Kiss, A. Chainani, S. Shin, M. Nohara and H. Takagi, *Science*, 2001, **294**, 2518–2520.

72 C. M. Pereira and W. Y. Liang, *J. Phys. C: Solid State Phys.*, 1982, **15**, L991.

73 J. C. Tsang, J. E. Smith and M. W. Shafer, *Phys. Rev. Lett.*, 1976, **37**, 1407–1410.

74 Y. Wu, M. An, R. Xiong, J. Shi and Q. M. Zhang, *J. Phys. D: Appl. Phys.*, 2008, **41**, 175408.

75 X. Xi, L. Zhao, Z. Wang, H. Berger, L. Forro, J. Shan and K. F. Mak, *Nat Nano*, 2015, **10**, 756–769.

76 F. Tuinstra and J. L. Koenig, *J. Chem. Phys.*, 1970, **53**, 1126–1130.

77 P. H. Tan, Y. M. Deng and Q. Zhao, *Phys. Rev. B*, 1998, **58**, 5435–5439.

78 S. Piscanec, M. Lazzeri, F. Mauri, A. C. Ferrari and J. Robertson, *Phys. Rev. Lett.*, 2004, **93**, 185503.

79 A. C. Ferrari, J. C. Meyer, V. Scardaci, C. Casiraghi, M. Lazzeri, F. Mauri, S. Piscanec, D. Jiang, K. S. Novoselov, S. Roth and A. K. Geim, *Phys. Rev. Lett.*, 2006, **97**, 187401.

80 L. Malard, M. Pimenta, G. Dresselhaus and M. Dresselhaus, *Physics Reports*, 2009, **473**, 51 – 87.

81 A. C. Ferrari, *Solid State Comm.*, 2007, **143**, 47–57.

82 C. R. Dean, A. F. Young, I. Meric, C. Lee, L. Wang, S. Sorgenfrei, K. Watanabe, T. Taniguchi, P. Kim, K. L. Shepard and J. Hone, *Nat. Nanotech.*, 2010, **5**, 722–726.

83 L. Song, L. Ci, H. Lu, P. B. Sorokin, C. Jin, J. Ni, A. G. Kvashnin, D. G. Kvashnin, J. Lou, B. I. Yakobson and P. M. Ajayan, *Nano Lett*, 2010, **10**, 3209–3215.

84 S. Sugai and T. Ueda, *Phys. Rev. B*, 1982, **26**, 6554–6558.

85 W.-D. Kong, S.-F. Wu, P. Richard, C.-S. Lian, J.-T. Wang, C.-L. Yang, Y.-G. Shi and H. Ding, *Appl. Phys. Lett.*, 2015, **106**, 081906.

86 Y. Feng, W. Zhou, Y. Wang, J. Zhou, E. Liu, Y. Fu, Z. Ni, X. Wu, H. Yuan, F. Miao, B. Wang, X. Wan and D. Xing, *Phys. Rev. B*, 2015, **92**, 054110.

87 M. Hangyo, S.-I. Nakashima and A. Mitsuishi, *Ferroelectrics*, 1983, **52**, 151–159.

88 L. Roubi and C. Carlone, *Phys. Rev. B*, 1988, **37**, 6808–6812.

89 S. G. Lyapin, A. N. Utyuzh, A. E. Petrova, A. P. Novikov, T. A. Lograsso and S. M. Stishov, *J. Phys.: Condens. Matter*, 2014, **26**, 396001.

90 E. Anastassakis and C. H. Perry, *J. Chem. Phys.*, 1976, **64**, 3604–3609.

91 A. Cingolani, M. Lugara and F. Levy, *Physica Scripta*, 1988, **37**, 389.

92 W. Unger, J. Reyes, O. Singh, A. Curzon, J. Irwin and R. Frindt, *Solid State Comm.*, 1978, **28**, 109 – 112.

93 S. Sugai, K. Murase, S. Uchida and S. Tanaka, *Solid State Comm.*, 1980, **35**, 433 – 436.

94 J. R. Duffey and R. D. Kirby, *Phys. Rev. B*, 1981, **23**, 1534–1541.

95 R. Samnakay, D. Wickramaratne, T. R. Pope, R. K. Lake, T. T. Salguero and A. A. Balandin, *Nano Lett.*, 2015, **15**, 2965–2973.

96 W. G. McMullan and J. C. Irwin, *Can. J. Php*, 1984, **62**, 789–795.

97 P. Kumar, A. Kumar, S. Saha, D. Muthu, J. Prakash, S. Patnaik, U. Waghmare, A. Ganguli and A. Sood, *Solid State Comm.*, 2010, **150**, 557 – 560.

98 H. Zeng, B. Zhu, K. Liu, J. Fan, X. Cui and Q. M. Zhang, *Phys. Rev. B*, 2012, **86**, 241301.

99 X. Ling, L. Liang, S. Huang, A. A. Puretzky, D. B. Geohegan, B. G. Sumpter, J. Kong, V. Meunier and M. S. Dresselhaus, *Nano Lett.*, 2015, **15**, 4080–4088.

100 H. Zhao, J. Wu, H. Zhong, Q. Guo, X. Wang, F. Xia, L. Yang, P. Tan and H. Wang, *Nano Res*, 2015, **8**, 3651–3661.

101 P. Nagler, G. Plechinger, C. Schuler and T. Korn, *physica status solidi (RRL)*, 2015, **9999**, n/a.

102 R. He, J.-A. Yan, Z. Yin, Z. Ye, G. Ye, J. Cheng, J. Li and C. H. Lui, *Nano Lett.*, 0, **0**, null.

103 X. Zhang, W.-P. Han, X.-F. Qiao, Q.-H. Tan, Y.-F. Wang, J. Zhang and P.-H. Tan, *Carbon*, 2016, **99**, 118 – 122.

104 C. H. Lui, Z. Ye, C. Ji, K.-C. Chiu, C.-T. Chou, T. I. Andersen, C. Means-Shively, H. Anderson, J.-M. Wu, T. Kidd, Y.-H. Lee and R. He, *Phys. Rev. B*, 2015, **91**, 165403.

105 J. L. Feldman, *J. Phys. Chem. Solids*, 1981, **42**, 1029.

106 M. Gatulle, M. Fischer and A. Chevy, *Phys. Status Solidi B*, 1983, **119**, 327–336.

107 R. Nicklow, N. Wakabayashi and H. G. Smith, *Phys. Rev. B*, 1972, **5**, 4951–4962.

108 J. Feng, X. F. Qian, C. W. Huang and J. Li, *Nat. Photonics*, 2012, **6**, 865–871.

109 S. Horzum, H. Sahin, S. Cahangirov, P. Cudazzo, A. Rubio, T. Serin and F. M. Peeters, *Phys. Rev. B*, 2013, **87**, 125415.

110 H. Sahin, S. Tongay, S. Horzum, W. Fan, J. Zhou, J. Li, J. Wu and F. M. Peeters, *Phys. Rev. B*, 2013, **87**, 165409.

111 A. A. Puretzky, L. Liang, X. Li, K. Xiao, K. Wang, M. Mahjouri-Samani, L. Basile, J. C. Idrobo, B. G. Sumpter, V. Meunier and D. B. Geohegan, *ACS Nano*, 2015, **9**, 6333–6342.

112 J.-U. Lee, K. Kim, S. Han, G. H. Ryu, Z. Lee and H. Cheong, *ACS Nano*, 0, **0**, null.

113 X. Lu, M. I. B. Utama, J. Lin, X. Luo, Y. Zhao, J. Zhang, S. T. Pantelides, W. Zhou, S. Y. Quek and Q. Xiong, *Adv. Mater.*, 2015, **27**, 4502–4508.

114 K. Liu, L. Zhang, T. Cao, C. Jin, D. Qiu, Q. Zhou, A. Zettl, P. Yang, S. G. Louie and F. Wang, *Nat Comm.*, 2014, **5**, 4966.

115 A. A. Puretzky, L. Liang, X. Li, K. Xiao, B. G. Sumpter, V. Meunier and D. B. Geohegan, *ACS Nano*, 2016, **0**, null.

116 X. Wang, A. M. Jones, K. L. Seyler, V. Tran, Y. Jia, H. Zhao, H. Wang, L. Yang, X. Xu and F. Xia, *Nat Nano*, **10**, 517–521.

117 C. H. Lui, Z. Ye, C. Keiser, E. B. Barros and R. He, *Appl. Phys. Lett.*, 2015, **106**, 041904.

118 X. Luo, C. Cong, X. Lu, T. Yu, Q. Xiong and S. Y. Quek, *Sci. Rep.*, 2015, **5**, 14565.

119 F. Xia, H. Wang and Y. Jia, *Nat Comm.*, 2014, **5**, 458.

120 L. Li, Y. Yu, G. J. Ye, Q. Ge, X. Ou, H. Wu, D. Feng, X. H. Chen and Y. Zhang, *Nat Nano*, 2014, **9**, 372–377.

121 J. Qiao, X. Kong, Z.-X. Hu, F. Yang and W. Ji, *Nat Comm.*, 2014, **5**, 4475.

122 F. Liu, S. Zheng, X. He, A. Chaturvedi, J. He, W. L. Chow, T. R. Mion, X. Wang, J. Zhou, Q. Fu, H. J. Fan, B. K. Tay, L. Song, R.-H. He, C. Kloc, P. M. Ajayan and Z. Liu, *Adv. Funct. Mater.*, 2015, n/a–n/a.

123 E. Zhang, Y. Jin, X. Yuan, W. Wang, C. Zhang, L. Tang, S. Liu, P. Zhou, W. Hu and F. Xiu, *Adv. Funct. Mater.*, 2015, **25**, 4076–4082.

124 D. Wolverson, S. Crampin, A. S. Kazemi, A. Ilie and S. J. Bending, *ACS Nano*, 2014, **8**, 11154–11164.

125 D. A. Chenet, O. B. Aslan, P. Y. Huang, C. Fan, A. M. van der Zande, T. F. Heinz and J. C. Hone, *Nano Lett.*, 2015, **15**, 5667–5672.

126 Y.-C. Lin, H.-P. Komsa, C.-H. Yeh, T. Bjorkman, Z.-Y. Liang, C.-H. Ho, Y.-S. Huang, P.-W. Chiu, A. V. Krasheninnikov and K. Suenaga, *ACS Nano*, 2015, **9**, 11249–11257.

127 H.-X. Zhong, S. Gao, J.-J. Shi and L. Yang, *Phys. Rev. B*, 2015, **92**, 115438.

128 H. B. Ribeiro, M. A. Pimenta, C. J. S. de Matos, R. L. Moreira, A. S. Rodin, J. D. Zapata, E. A. T. de Souza and A. H. C. Neto, *ACS Nano*, 2015, **9**, 4270–4276.

129 J. Wu, N. Mao, L. Xie, H. Xu and J. Zhang, *Angew. Chem.*, 2015, **127**, 2396–2399.

130 X. Luo, X. Lu, G. K. W. Koon, A. H. C. Neto, B. Ozyilmaz, Q. Xiong and S. Y. Quek, *Nano Lett.*, 2015, **15**, 3931–3938.

131 X.-F. Qiao, J.-B. Wu, L.-W. Zhou, J.-S. Qiao, W. Shi, T. Chen, X. Zhang, J. Zhang, W. Ji and P.-H. Tan, *arXiv:1512.08935*, 2015.

132 E. Lorchat, G. Froehlicher and S. Berciaud, *arxiv:1512.03842*, 2015.

Nanoscale Accepted Manuscript